Toward a K-Profile Parameterization of Langmuir Turbulence in Shallow Coastal Shelves

NITYANAND SINHA, ANDRES E. TEJADA-MARTÍNEZ, AND CIGDEM AKAN

University of South Florida, Tampa, Florida

CHESTER E. GROSCH

Ocean, Earth and Atmospheric Sciences, and Center for Coastal Physical Oceanography, Old Dominion University, Norfolk, Virginia

(Manuscript received 5 August 2014, in final form 11 May 2015)

ABSTRACT

Interaction between the wind-driven shear current and the Stokes drift velocity induced by surface gravity waves gives rise to Langmuir turbulence in the upper ocean. Langmuir turbulence consists of Langmuir circulation (LC) characterized by a wide range of scales. In unstratified shallow water, the largest scales of Langmuir turbulence engulf the entire water column and thus are referred to as full-depth LC. Large-eddy simulations (LESs) of Langmuir turbulence with full-depth LC in a wind-driven shear current have revealed that vertical mixing due to LC erodes the bottom log-law velocity profile, inducing a profile resembling a wake law. Furthermore, in the interior of the water column, two sources of Reynolds shear stress, turbulent (nonlocal) transport and local Stokes drift shear production, can combine to lead to negative mean velocity shear. Meanwhile, near the surface, Stokes drift shear serves to intensify small-scale eddies leading to enhanced vertical mixing and disruption of the surface log law. A K-profile parameterization (KPP) of the Reynolds shear stress comprising local and nonlocal components is introduced, capturing these basic mechanisms by which Langmuir turbulence in unstratified shallow water impacts the vertical mixing of momentum. Single-water-column, Reynolds-averaged Navier–Stokes simulations with the new parameterization are presented, showing good agreement with LES in terms of mean velocity. Results show that coefficients in the KPP may be parameterized based on attributes of the full-depth LC.

1. Introduction

Interaction between Stokes drift velocity generated by surface gravity waves and the wind-driven shear current gives rise to Langmuir turbulence in the upper ocean, characterized by Langmuir circulation (LC) across a wide range of spatial and temporal scales. LC consists of parallel counterrotating vortices aligned in the direction of the wind ranging in scale from centimeters to kilometers in the downwind direction. The largest of the LC scales can extend down to the base of the upper-ocean mixed layer. In shallow shelves, during times when the water column is unstratified (such as during the passage of storms), the largest scales of LC have been observed engulfing the entire water column, serving as a dominant mechanism for sediment resuspension (Gargett et al. 2004; Gargett and Wells 2007; Savidge et al. 2008). Large-eddy simulations (LESs) of Langmuir turbulence in unstratified shallow water have revealed significant influences of this turbulence regime on the dynamics of surface and bottom boundary layers and the core (bulk) flow region (Tejada-Martínez and Grosch 2007; Tejada-Martínez et al. 2012, 2013; Akan et al. 2013; Kukulka et al. 2011, 2012). For example, Akan et al. (2013) and Tejada-Martínez et al. (2013) have shown that Stokes drift shear (the mechanism generating Langmuir turbulence) acts to intensify near-surface, small-scale eddies, ultimately leading to enhanced vertical mixing in this region and a departure from classical surface log-layer dynamics. Furthermore, near-bottom mixing induced by full-depth Langmuir cells can lead to a departure from classical bottom log-layer dynamics (Tejada-Martínez et al. 2012). Finally, as will be shown via LESs in the current study, turbulent (nonlocal) transport and local Stokes drift shear production of Reynolds shear stress (i.e., turbulent vertical momentum flux) in

Corresponding author address: Andres E. Tejada-Martínez, Civil and Environmental Engineering, University of South Florida, 4202 E. Fowler Ave., ENB 118, Tampa, FL 33620.
E-mail: aetejada@usf.edu

DOI: 10.1175/JPO-D-14-0158.1

the Langmuir turbulence regime can combine to lead to negative vertical shear in the mean velocity in the interior of the water column.

The previously described LES simulations have been facilitated by the inclusion of the well-known Craik–Leibovich (CL) vortex force (Craik and Leibovich 1976) into the governing momentum equations in order to account for the interaction between Stokes drift and the wind-driven current generating Langmuir turbulence without having to resolve surface gravity waves.

LES simulations of Langmuir turbulence in the upper-ocean mixed layer (e.g., Skyllingstad and Denbo 1995; McWilliams et al. 1997; Li et al. 2005) and in shallow water (Tejada-Martínez and Grosch 2007; Kukulka et al. 2011) have revealed a Langmuir turbulence structure vastly different than the classical shear-dominated turbulence structure. These differences have underscored the need to develop turbulence parameterizations for ocean models able to capture the effects of Langmuir turbulence. Efforts toward the inclusion of the effect of Langmuir turbulence in parameterizations of vertical mixing in upper-ocean models date back to the late 1990s and 2000s. D'Alessio et al. (1998) and Kantha and Clayson (2004) included the CL vortex force in the momentum equation of a single-water-column, upper-ocean mixed-layer model and in the model's two-equation turbulence scheme, specifically, the turbulent kinetic energy k and the kl equations (where l is the turbulent length scale) . More recently, Harcourt (2013) revisited these models and included the terms associated with the CL vortex force in the algebraic Reynolds stress model equations used to derive the stability functions that premultiply the eddy viscosity and eddy diffusivity arising from k and l. McWilliams and Sullivan (2000) proposed a K-profile parameterization (KPP; Large et al. 1994) of turbulent vertical scalar flux with an enhanced velocity scale and a nonlocal component accounting for Langmuir turbulence. Parameters associated with the velocity-scale enhancement and the nonlocal component were calibrated by fitting the KPP-predicted eddy viscosity with an LES-predicted eddy viscosity. Smyth et al. (2002) extended the KPP of McWilliams and Sullivan (2000) to the Reynolds shear stress or turbulent vertical momentum flux.

The necessity of including the effects of Langmuir circulation and turbulence in the mixing/dissipation parameterization of global climate models has been emphasized by Belcher et al. (2012), who showed that parameterizations of turbulent mixing currently used in these models lead to substantial and systematic errors in the computed depth of the ocean surface boundary layers. They concluded that surface-wave-forced Langmuir turbulence, which is not included in current parameterizations, is an important physical process in the ocean surface boundary layer and must be included in the parameterization. Very recently, D'Asaro (2014) showed that observations in the ocean are consistent with Langmuir turbulence, not wave breaking, being the dominant mechanism by which waves generate turbulence in the ocean surface boundary layer and thus must be included in the turbulence parameterization.

To build an accurate parameterization of the effect of Langmuir turbulence on vertical mixing of momentum and hence the mean streamwise velocity profile, the changes in this profile must be known. More specifically, the dominant effects, for example, the erosion of the log-layer profile; the increase in the energy of small-scale near-surface eddies; and changes in the nonlocal transport of the Reynolds shear stress, by which Langmuir turbulence modifies the mean streamwise velocity profile, must be known in order to incorporate them into the model. For this reason, this study reviews the mechanisms described above by which Langmuir turbulence in shallow water and associated full-depth Langmuir circulation affect vertical mixing in unstratified water columns, as uncovered via LES. Then a KPP is formulated that is capable of representing these key mechanisms. The KPP is implemented within a single-water-column model of Langmuir turbulence in shallow water, and mean velocity predicted by the model is shown to be in excellent agreement with LESs. It is also shown that coefficients in the KPP can be calibrated and may be ultimately parameterized using LESs or field measurements, as they are linked to physical attributes of the full-depth LC.

2. Governing LES equations

To understand core flow dynamics and near-bottom and near-surface boundary layer dynamics in the presence of Langmuir turbulence with full-depth LC, LESs of wind-driven shallow water have been performed. Interaction between Stokes drift velocity induced by surface gravity waves and the wind-driven shear current leads to the generation of Langmuir turbulence characterized by LC. The governing equations for LESs of Langmuir turbulence are the filtered continuity and Navier–Stokes equations augmented with the CL vortex force (Craik and Leibovich 1976), the latter force serving to parameterize the generating mechanism for Langmuir turbulence without having to directly resolve the surface gravity waves.

a. *Spatially filtered Navier–Stokes equation (CL equation)*

The nondimensional, low-pass spatially and time-filtered continuity and Navier–Stokes equations augmented with the CL vortex force can be written as

$$\frac{\partial \overline{u}_i}{\partial x_i} = 0 \qquad (1)$$

and

$$\frac{\partial \overline{u}_i}{\partial t} + \overline{u}_j \frac{\partial \overline{u}_i}{\partial x_j} = -\frac{\partial \overline{\Pi}}{\partial x_i} + \frac{1}{\mathrm{Re}_\tau} \frac{\partial^2 \overline{u}_i}{\partial x_j^2} - \frac{\partial \tau_{ij}^{\mathrm{LES}}}{\partial x_j} + \frac{1}{\mathrm{La}_t^2} \varepsilon_{ijk} U_j^s \overline{\omega}_k , \qquad (2)$$

where ε_{ijk} is the totally antisymmetric third-rank tensor and the overbar denotes the application of low-pass space and time filters. The filter consists of the spatial filter in traditional LESs compounded with a time filter for the purpose of filtering out the surface gravity waves, as per the CL (Craik and Leibovich 1976) formulation. Variables $\overline{u}_i$ and $\overline{\omega}_i$ are the filtered ith component of velocity and vorticity in a Cartesian coordinate system (x_1, x_2, x_3). The space and time-filtered modified pressure is denoted as $\overline{\Pi}$. The exact expression for $\overline{\Pi}$ in terms of the original pressure and the Stokes drift velocity is defined by McWilliams et al. (1997):

$$\overline{\Pi} = \overline{P} + \frac{1}{2}\Lambda,$$
$$\Lambda = \frac{1}{\mathrm{La}_t^4} U_i^s U_i^s + \frac{1}{\mathrm{La}_t^2} \overline{u}_i U_i^s , \qquad (3)$$

where $\overline{P}$ is the space- and time-filtered pressure and U_i^s denotes the predetermined dimensionless Stokes drift velocity induced by surface waves.

The CL vortex force is the last term in Eq. (2), consisting of the Stokes drift velocity crossed with the flow vorticity.

These equations have been made dimensionless with water column half-depth δ and friction velocity u_τ. Friction velocity u_τ is associated with wind stress τ_w and can be expressed as $u_\tau = \sqrt{\tau_w/\rho}$, where ρ is the density of the water. Friction Reynolds number ($\mathrm{Re}_\tau = u_\tau\delta/\nu$, where ν is the molecular viscosity) is a measure of the strength of advection relative to diffusion.

The turbulent Langmuir number La_t appearing in the dimensionless CL equation [Eq. (2)] consists of the ratio of friction velocity u_τ to characteristic Stokes drift velocity U_0 and is expressed as $\mathrm{La}_t = \sqrt{u_\tau/U_0}$, where $U_0 = \omega k a^2$, with ω as the dominant frequency, k as the dominant wavenumber (inversely proportional to the dominant wavelength λ), and a as the dominant amplitude of the surface gravity waves generating Langmuir turbulence [see Gargett and Wells (2007) for calculation of these wave characteristics from field measurements]. Note that the dominant wavenumber of surface gravity waves is $k = 2\pi/\lambda$. The turbulent Langmuir number La_t is inversely proportional to the strength of wave forcing relative to wind forcing. Note that for the intermediate-depth water waves considered in the present study, U_0 in the definition of La_t does not correspond to the Stokes drift velocity at the surface, as it would for deep-water waves (see Phillips 1967).

The nondimensional Stokes drift velocity appearing in Eq. (2) is taken to be nonzero only in the downwind (x_1) direction and is defined by Phillips (1967) as

$$U_1^s = \frac{\cosh[2\tilde{k}(x_3+1)]}{2\sinh^2(2\tilde{k})} \quad \text{and} \quad U_2^s = U_3^s = 0. \qquad (4)$$

In the previous expressions, $\tilde{k} = k\delta$ is the dimensionless wavenumber, and the dimensionless vertical coordinate x_3 extends from -1 at the bottom of the water column to $+1$ at the surface in the wind-driven shear flow simulations, to be presented in upcoming sections. Furthermore, the Stokes drift velocity profile in Eq. (4) decays with depth; its decay rate is inversely proportional to the dominant wavelength of the surface waves, λ.

The LES subgrid-scale (SGS) stress τ_{ij}^{LES} is generated by spatial filtering of the momentum equation and is modeled using the eddy viscosity-based dynamic Smagorinsky model as

$$\tau_{ij}^{\mathrm{LES}} = 2\nu_t^{\mathrm{LES}} \overline{S}_{ij} , \qquad (5)$$

where the eddy viscosity is $\nu_t^{\mathrm{LES}} = (C_s\overline{\Delta})^2|\overline{S}|$, with C_S denoting the Smagorinsky coefficient; $\overline{\Delta}$ denoting the width of the low pass spatial LES filter; $|\overline{S}|$ denoting the norm of the filtered strain-rate tensor, defined as $|\overline{S}| = (2\overline{S}_{ij}\overline{S}_{ij})^{1/2}$; and $\overline{S}_{ij}$ denoting the filtered strain-rate tensor $\overline{S}_{ij} = (\overline{u}_{i,j} + \overline{u}_{j,i})/2$. Note that in practice, the low-pass filter used to obtain the spatially filtered equations in Eq. (2) is implicitly set by an undefined combination of the numerical method and the grid discretizing the filtered equations. Thus, typically $\overline{\Delta}$ is representative of the characteristic grid cell size. In this study, model coefficient $(C_s\overline{\Delta})^2$ is computed dynamically as described by Lilly (1992).

All flow variables and equations have been specified in dimensionless form for ease of presentation of important dimensionless parameters such as Re_τ and La_t. Henceforth, all variables are taken as dimensional unless specified otherwise.

b. Flow configuration

The flow domain for the LES in this study is shown in Fig. 1. The flow is subjected to constant wind shear stress at the surface with zero normal flow. The surface stress is prescribed in such a way that the friction Reynolds number is $\mathrm{Re}_\tau = 395$. Although in the coastal ocean Langmuir turbulence occurs under much higher

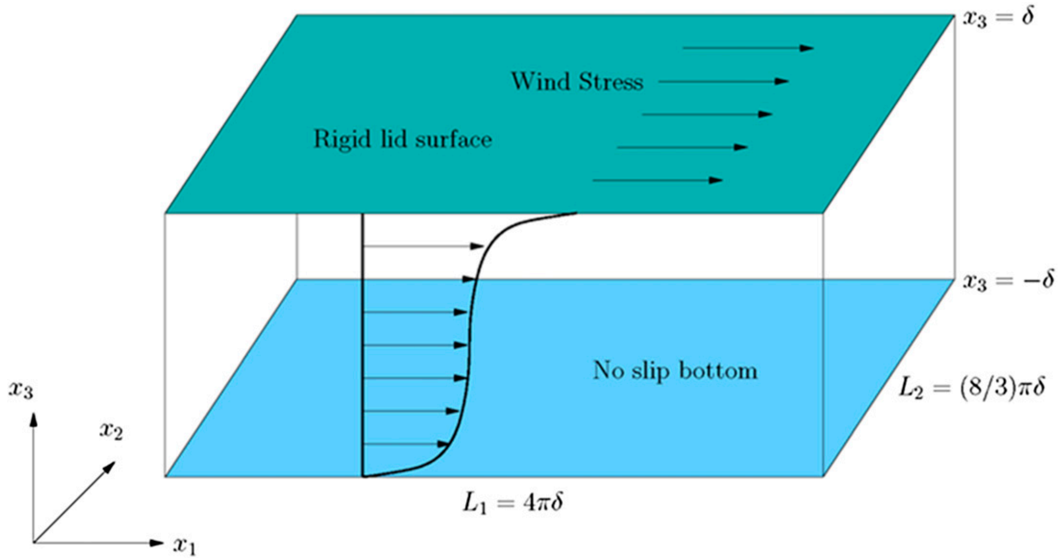

FIG. 1. Computational domain and boundary conditions.

Reynolds numbers [of $O(100\,000)$], Tejada-Martínez et al. (2009) have shown that the turbulence simulated at a lower Reynolds number such as $\mathrm{Re}_\tau = 395$ is able to scale up favorably to the turbulence measured in the field by Gargett and Wells (2007). This was done by redimensionalizing the LES velocity solution with wind stress friction velocity (u_τ) and water column half depth (δ) of the field measurements.

A no-slip boundary condition is applied at the bottom wall of the domain in Fig. 1. For this configuration, the mean wall shear stress computed at the bottom is equal to the imposed wind stress at the top of the domain once the flow has reached statistical equilibrium. Boundary conditions are periodic in horizontal directions (x_1 and x_2). The latter condition is representative of a costal shelf region far from (unaffected by) lateral boundaries.

The domain size in x_1 (downwind) and x_2 (crosswind) directions is $4\pi\delta$ and $8\pi\delta/3$, respectively. In the vertical (x_3) direction, the water depth is $H = 2\delta$. The crosswind domain size $8\pi\delta/3$ is expected to be sufficiently wide to be able to resolve one full-depth Langmuir cell. This length ($8\pi\delta/3 \approx 4H$) falls within the range of values reported for spanwise (crosswind) length of one full-depth Langmuir cell ($3H$–$6H$) during the field observations of Gargett et al. (2004) and Gargett and Wells (2007).

The LES computational grid for flows with and without CL vortex forcing (i.e., with and without Langmuir turbulence) contains 32, 64, and 97 points in the x_1, x_2, and x_3 directions, respectively. This grid is uniform in the x_1 and x_2 directions; however, in the vertical direction (x_3) the grid is highly stretched using a hyperbolic function in order to resolve the bottom and surface viscous boundary layers. The grid stretching is symmetric about middepth in the vertical direction; thus, both surface and bottom viscous boundary layers have the same resolution. In all simulations the first grid point off the wall or the surface is at a distance $x_3^+ = 1$, so the viscous sublayers ($0 < x_3^+ < 7$) are adequately resolved. Note that x_3^+ is a measure of the distance to the boundary (surface or bottom of the water column) in wall units (i.e., $x_3^+ = z\mathrm{Re}_\tau$), where z is the dimensionless distance to the bottom or to the surface.

The governing equations in Eqs. (1) and (2) within the previously described domain configuration were solved using the hybrid spectral/finite-difference solver of Tejada-Martínez and Grosch (2007), in which horizontal (x_1 and x_2) directions are discretized using fast Fourier transforms and the vertical (x_3) direction is discretized using fifth- and sixth-order compact finite-difference schemes.

In the upcoming sections, results from wind-driven flows with or without Langmuir turbulence (i.e., with or without CL vortex forcing) in statistical equilibrium are presented. The flow without LC or CL forcing is referred to as $\mathrm{La}_t = \infty$. Four simulations of flows with LC have been performed and corresponding wind and wave forcing parameters are summarized in Table 1. Main parameter inputs to the CL vortex force appearing in the LES

TABLE 1. Summary of wind and wave forcing parameters in simulations. Here, NA indicates that a value is not applicable.

Case I	$\mathrm{La}_t = \infty$	$\lambda = \mathrm{NA}$	Flow without CL vortex forcing
Case II	$\mathrm{La}_t = 0.7$	$\lambda = 6H$	Flow with CL vortex forcing
Case III	$\mathrm{La}_t = 0.4$	$\lambda = 6H$	
Case IV	$\mathrm{La}_t = 1.0$	$\lambda = 6H$	
Case V	$\mathrm{La}_t = 0.7$	$\lambda = 4H/3$	

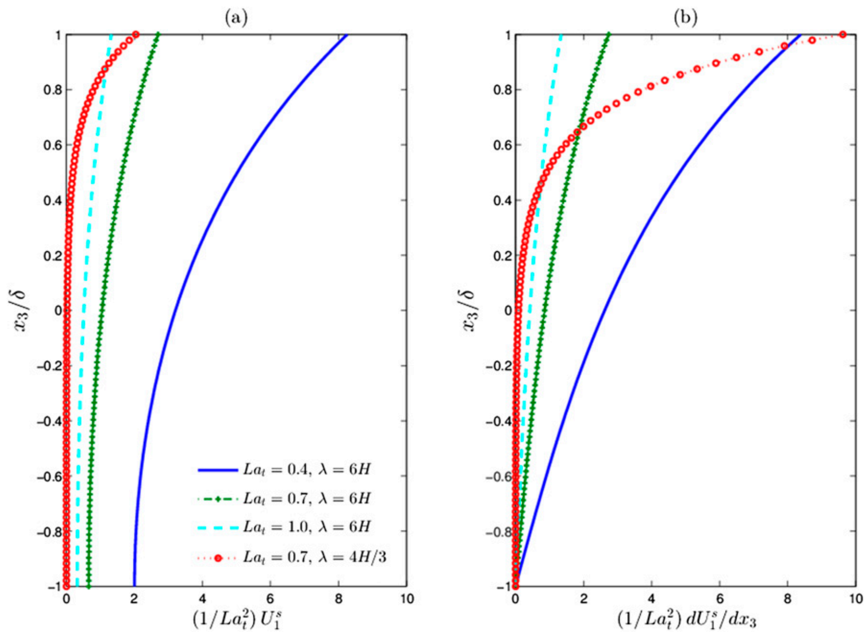

FIG. 2. (a) Stokes drift velocity and (b) Stokes drift velocity vertical shear.

equations are the turbulent Langmuir number La_t, representative of wind forcing relative to wave forcing, and λ, the dominant wavelength of surface gravity waves generating Langmuir turbulence. Case II in Table 1, with $\mathrm{La}_t = 0.7$ and $\lambda = 12\delta = 6H$, corresponds to the wind and wave forcing conditions during the full-depth LC field measurements of Gargett et al. (2004) and Gargett and Wells (2007). Note that wavelength $\lambda = 12\delta = 6H$ represents a shallow/intermediate surface wave and $\lambda = 8\delta = 4H/3$ corresponds to a short (deep water) wave. Figure 2 shows depth profiles of the Stokes drift velocity (appearing in the CL vortex force) and Stokes drift vertical shear. Stokes drift shear is important because it serves as the source for the generation of Langmuir turbulence, as can be seen from the transport equation for downwind vorticity derived from the momentum equation with CL vortex forcing (Holm 1996).

3. LES results

a. Turbulence structure

In Langmuir turbulence in homogenous shallow water, the largest, most coherent, and most persistent scales of this turbulence regime consist of full-depth LC. Next, the largest structures in wind-driven flows with and without Langmuir turbulence (i.e., with and without LC) are described. Note that throughout the rest of this study, the terminology "with LC" and "without LC" are taken to be equivalent to "with Langmuir turbulence" and "without Langmuir turbulence," respectively. This is done here because historically Langmuir turbulence has been referred to as Langmuir circulation.

Flow without LC is characterized by Couette cells. Similar to full-depth Langmuir cells but weaker in coherency, Couette cells are parallel counterrotating vortices aligned in the direction of the wind engulfing most of the water column (Papavassiliou and Hanratty 1997; Tejada-Martínez and Grosch 2007; Kukulka et al. 2012).

Couette and full-depth Langmuir cells are coherent in the downwind direction (x_1). This suggests averaging velocity fluctuations over x_1 in order to stress coherency in this direction. This also helps reveal the crosswind (x_2)–vertical (x_3) variation of these full-depth structures.

Figures 3–6 show the x_2–x_3 variation of all three components of x_1-averaged (partially averaged) velocity fluctuations in wind-driven flows with and without CL vortex forcing (i.e., with and without LC). All flows with CL vortex forcing (Figs. 3d–f and Figs. 4–6) are characterized by a full-depth, one-cell structure in close agreement with the full-depth Langmuir cells observed in the field measurements of Gargett and Wells (2007) and Gargett et al. (2004). For example, the single-cell structure in the flows with CL vortex forcing possesses a crosswind width $\approx 4H(8\delta)$ consistent with the field measurements of Gargett and Wells (2007). Note that although the computational domain size in the crosswind direction was chosen following the expected full-depth Langmuir cell crosswind width as described earlier, it has been confirmed that the crosswind length of the domain does not set (or force) the crosswind length of the resolved full-depth Langmuir cell. Confirmation

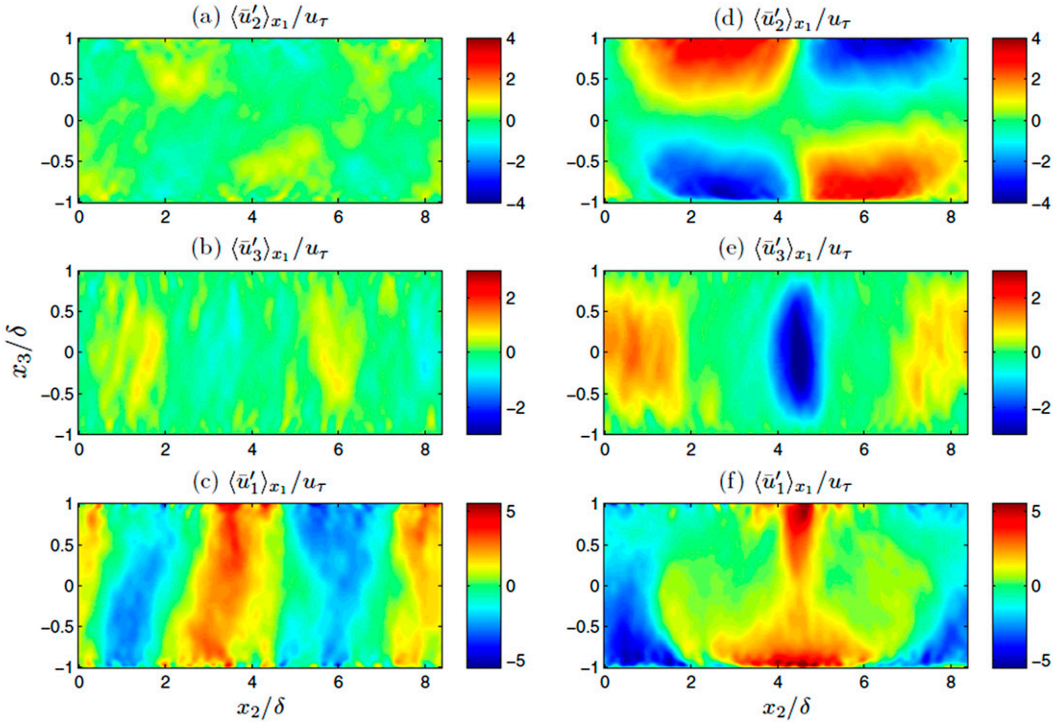

FIG. 3. Instantaneous velocity fluctuations averaged over the downwind (x_1) direction (a)–(c) in flows without LC and in flows (d)–(f) with LC with $\mathrm{La}_t = 0.7$ and $\lambda = 6H$. (Top) crosswind velocity fluctuation, (middle) vertical velocity fluctuation, and (bottom) downwind fluctuation.

was made by Tejada-Martínez and Grosch (2007) by performing LES of wind-driven flow with CL vortex forcing in which the crosswind length of the domain was double the length of the one chosen here. In that simulation they were able to resolve two full-depth Langmuir cells, each with crosswind width consistent with the measurements of Gargett and Wells (2007) and Gargett et al. (2004). Other favorable comparisons between flows with CL vortex forcing and field measurements during episodes of full-depth LC are described by Tejada-Martínez and Grosch (2007) and Tejada-Martínez et al. (2009). Here we focus on the impact of wind and wave forcing parameters (La_t and λ) on the structure of the full-depth Langmuir cell that had not been explored in the earlier studies.

In flows with LC, the partially averaged crosswind velocity fluctuation is intensified near the surface and exhibits a surface convergence zone corresponding to the surface convergence of the full-depth Langmuir cell (e.g., see Figs. 4a,d). Surface convergence leads to the generation of the LC full-depth downwelling limb, characterized by negative vertical velocity fluctuation (Figs. 4b,e). Furthermore, the downwelling limb coincides with a region of positive downwind velocity fluctuation (Figs. 4c,f) that serves to enhance the mean downwind current within this zone.

A decrease in turbulent Langmuir number from $\mathrm{La}_t = 1.0$ down to $\mathrm{La}_t = 0.7$ while holding the wavelength of surface waves constant at $\lambda = 6H$ leads to an intensification of the partially averaged velocity fluctuations associated with full-depth LC, especially in terms of crosswind velocity fluctuation at the surface and bottom of the water column (Figs. 4a,d). A decrease in La_t from 0.7 to 0.4 leads to a restructuring of the cell reflected through higher-averaged vertical velocities within the upwelling limb of the cell (Figs. 5b,e) as well as more intense crosswind velocity fluctuation at the surface, but less intense at the bottom (Figs. 5a,d) . Thus, relative to the cell with ($\mathrm{La}_t = 0.7, \lambda = 6H$), the cell with ($\mathrm{La}_t = 0.4, \lambda = 6H$) is deemed weaker in the lower half of the water column and stronger in the upper half. This will be quantified further below in terms of root-mean-square (rms) of vertical velocity fluctuation.

A decrease in λ from $6H$ to $4H/3$ with La_t fixed at 0.7 leads to less coherent full-depth LC, characterized by averaged velocity fluctuations weaker in magnitude, especially in terms of crosswind and vertical velocity fluctuations (see Figs. 6a,d and Figs. 6b,e, respectively). This is consistent with the magnitude of the CL vortex force and Stokes drift velocity shear decaying with depth faster for smaller values of λ (see Fig. 2). However, the case with ($\mathrm{La}_t = 0.7, \lambda = 4H/3$) is characterized by higher

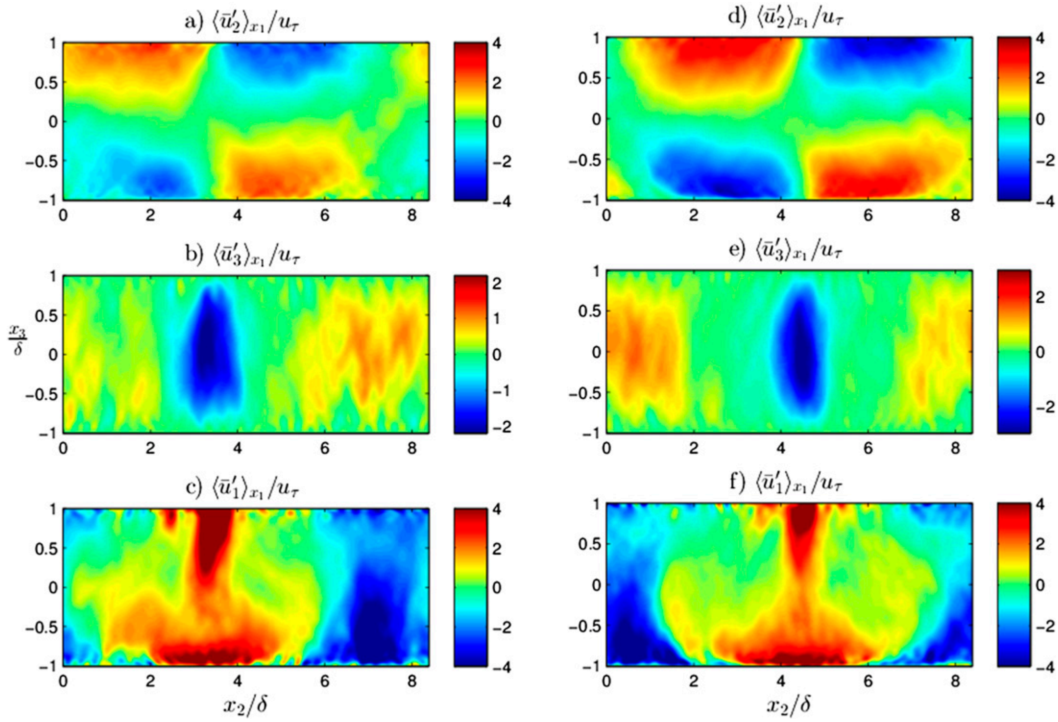

FIG. 4. As in Fig. 3, but for (a)–(c) flows with LC with $\mathrm{La}_t = 1.0$ and $\lambda = 6H$ and (d)–(f) flows with LC with $\mathrm{La}_t = 0.7$ and $\lambda = 6H$.

Stokes drift shear near the surface than the case with ($\mathrm{La}_t = 0.7, \lambda = 6H$; Fig. 2b). As will be described further below, the higher near-surface Stokes shear in the former leads to intensification of near-surface, small-scale vortices rather than intensification of the full-depth Langmuir cells.

Finally, note that the flow without the CL vortex force (i.e., flow without LC) is characterized by a two-cell structure (Figs. 3a–c) that is weaker and less coherent than the full-depth LC resolved in the flows with CL forcing. The two-cell structure is similar in size and structure to Couette cells resolved in the LES of Couette flow of Papavassiliou and Hanratty (1997). As noted by Papavassiliou and Hanratty, in Couette flow (flow between two parallel no-slip pates moving in opposite directions), the mean streamwise velocity is asymmetric; thus, production of turbulent kinetic energy by mean velocity vertical shear is everywhere nonzero from wall to wall. Such production favors the growth of near-wall turbulent structures outward toward the core region, and ultimately structures that extend from wall to wall. A similar turbulent kinetic energy production mechanism is also present in the wind-driven flow without LC, giving rise to similar Couette cells.

Simulations with LC previously described were initiated by turning on the CL vortex force when the wind-driven flow without LC (i.e., with Couette cells) was in statistical equilibrium. The CL vortex force caused a merging of the Couette cells, giving rise to the single full-depth Langmuir cell previously described once the flow achieved a new statistical equilibrium state (see Figs. 3a–c and Figs. 4d–f). Alternatively, simulations with CL vortex forcing were also initiated from rest. In these cases, the final statistical equilibrium state is the same obtained when the CL vortex force is turned on starting from the wind-driven Couette flow.

To highlight the intensification of near-surface turbulence intensity caused by increasing near-surface Stokes drift shear, mentioned earlier, consider a comparison in terms of rms of vertical velocity fluctuation $\langle \overline{u}_3' \overline{u}_3' \rangle^{1/2}$ between the LC flows with different La_t and λ. Figure 7a shows that the flow with ($\mathrm{La}_t = 0.7, \lambda = 4H/3$) is characterized by higher $\langle \overline{u}_3' \overline{u}_3' \rangle^{1/2}$ near the surface, compared to the flow with ($\mathrm{La}_t = 0.7, \lambda = 6H$). As originally noted by Akan et al. (2013), this can be attributed to intensification of small-scale, near-surface eddies in the former case (seen in Figs. 8b,c), despite the weaker full-depth cells in the $\lambda = 4H/3$ case compared to the $\lambda = 6H$ case (observed earlier in Fig. 6). Intensification of near-surface eddies in the ($\mathrm{La}_t = 0.7, \lambda = 4H/3$) case relative to the ($\mathrm{La}_t = 0.7, \lambda = 6H$) case is due to higher near-surface Stokes drift shear in the former (seen in Fig. 2). This

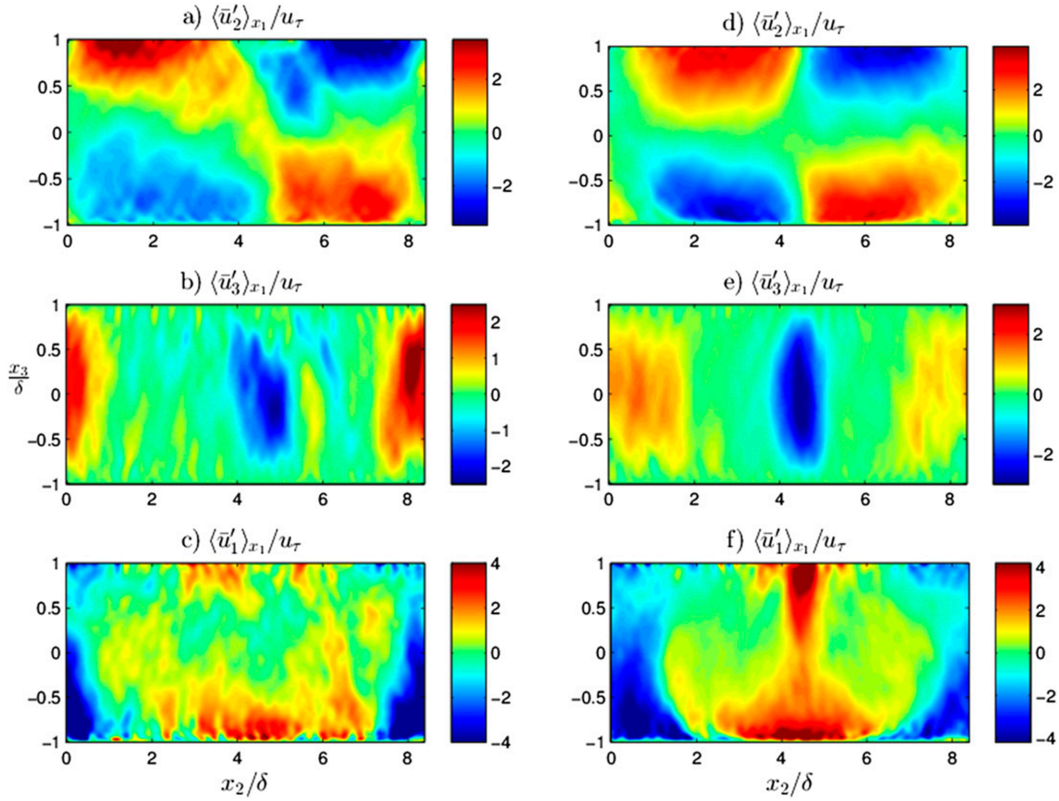

FIG. 5. As in Fig. 3, but for (a)–(c) flows with LC with $\mathrm{La}_t = 0.4$ and $\lambda = 6H$ and (d)–(f) flows with LC with $\mathrm{La}_t = 0.7$ and $\lambda = 6H$.

intensification of near-surface, small-scale eddies by Stokes drift shear is ultimately responsible for increasing near-surface mixing, suggesting that a parameterization of Langmuir turbulence should be characterized by an enhanced near-surface eddy viscosity, as will be developed in this study.

Comparing flow without LC and flow with LC with ($\mathrm{La}_t = 0.7$, $\lambda = 6H$) in Fig. 7a and in Figs. 8a and 8b, it can be seen that Stokes drift shear in the LC case is not sufficiently high to increase the intensity of near-surface small eddies and only serves to generate Langmuir turbulence and thus full-depth LC.

Figure 7b shows $\langle \overline{u}_3' \overline{u}_3' \rangle_{\mathrm{CC}}^{1/2}$ defined as the contribution from coherent cells (either full-depth Langmuir cells or Couette cells) to overall vertical velocity rms $\langle \overline{u}_3' \overline{u}_3' \rangle^{1/2}$. The contribution $\langle \overline{u}_3' \overline{u}_3' \rangle_{\mathrm{CC}}^{1/2}$ is computed using a triple decomposition of resolved velocity (Tejada-Martínez and Grosch 2007; Akan et al. 2013), leading to

$$\langle \overline{u}_3' \overline{u}_3' \rangle_{\mathrm{CC}}^{1/2} = \langle \langle \overline{u}_3' \rangle_{t,x_1} \langle \overline{u}_3' \rangle_{t,x_1} \rangle^{1/2}. \tag{6}$$

In this expression the interior brackets denote a partial Reynolds averaging over time and downwind direction (x_1) (the latter being the same averaging used to define the partially averaged fluctuations in Figs. 3–6). The outer bracket in Eq. (6) denotes full Reynolds averaging over time in the downwind (x_1) and crosswind (x_2) directions.

Figure 7b shows that the vertical velocity rms associated with full-depth LC is much less in the case with ($\mathrm{La}_t = 0.7$, $\lambda = 4H/3$) than in the cases with ($\mathrm{La}_t = 0.7$, $\lambda = 6H$) and ($\mathrm{La}_t = 0.4$, $\lambda = 6H$). This is consistent with Fig. 5 and 6 discussed earlier, showing that the strength of full-depth LC in the case with $\lambda = 4H/3$ is weaker than in the two other cases with $\lambda = 6H$.

Comparing the cases with ($\mathrm{La}_t = 0.7$, $\lambda = 6H$) and ($\mathrm{La}_t = 0.4$, $\lambda = 6H$) in terms of $\langle \overline{u}_3' \overline{u}_3' \rangle_{\mathrm{CC}}^{1/2}$, it can be concluded that the full-depth LC in the latter case is stronger in the upper half of the water column and vice versa in the lower half. This is consistent with the partially averaged crosswind velocity fluctuations in Fig. 5 exhibiting a more intense (less intense) surface convergence (bottom divergence) of the full-depth LC in the ($\mathrm{La}_t = 0.4$, $\lambda = 6H$) case.

Although there are differences between the cases with ($\mathrm{La}_t = 0.7$, $\lambda = 6H$) and ($\mathrm{La}_t = 0.4$, $\lambda = 6H$) in terms of $\langle \overline{u}_3' \overline{u}_3' \rangle_{\mathrm{CC}}^{1/2}$ in Fig. 7b, these differences are not as pronounced as the differences in terms of $\langle \overline{u}_3' \overline{u}_3' \rangle^{1/2}$ seen in

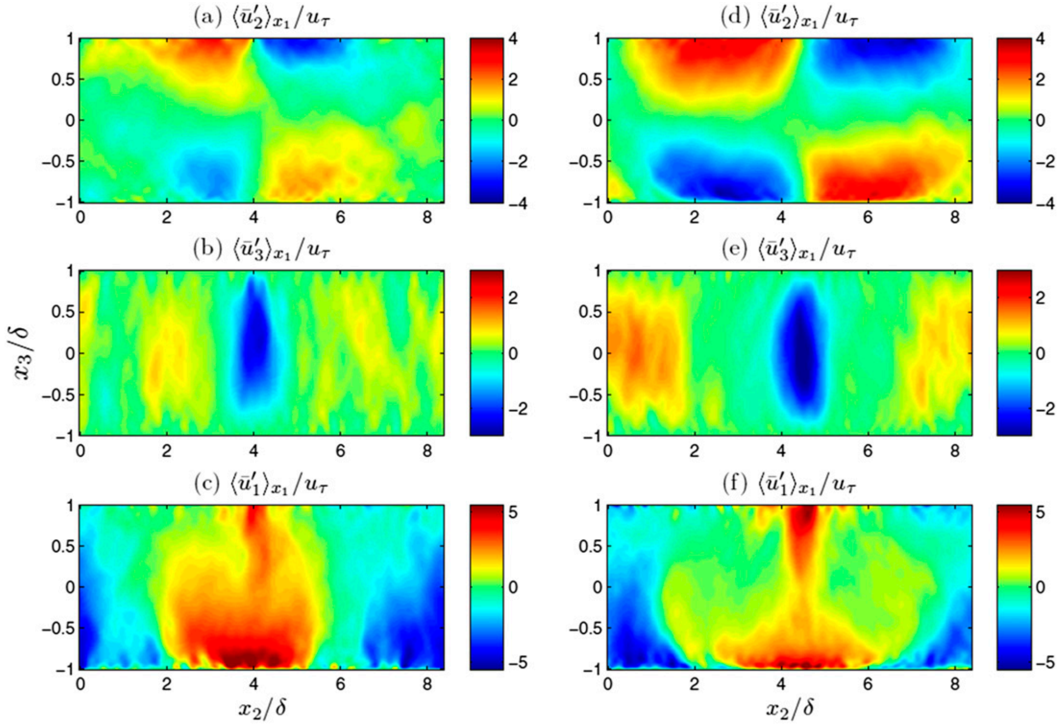

FIG. 6. As in Fig. 3, but for (a)–(c) flows with LC with $\mathrm{La}_t = 0.7$ and $\lambda = 4H/3$ and (d)–(f) flows with LC with $\mathrm{La}_t = 0.7$ and $\lambda = 6H$.

Fig. 7a. This suggests that a decrease in La_t from 0.7 to 0.4 with fixed λ gives rise to intensification of Langmuir turbulence scales of smaller size and less coherent than the full-depth LC. Intensification of these smaller Langmuir turbulence scales is due to the increase in Stokes drift shear throughout the entire water column induced by lowering La_t from 0.7 to 0.4 with λ fixed at $6H$; recall Fig. 2b).

Finally, Fig. 7b shows that the vertical velocity rms associated with Couette cells is much less than the vertical velocity rms associated with full-depth LC, consistent with Couette cells being less coherent than full-depth LC, as shown earlier through Figs. 3–6.

b. *Mean velocity*

1) DISRUPTION OF THE SURFACE LOG LAW

Next, the impact of shallow-water Langmuir turbulence within the near-surface log layer is examined in terms of mean velocity. In all flows with LC, the Langmuir turbulence and associated full-depth LC homogenize momentum throughout most of the water column (relative to flow without LC), which leads to near-constant mean downwind velocity profiles, as seen in Fig. 9a. Figure 9b shows mean downwind velocity deficit in the upper half of the water column. Mean downwind velocity deficit is defined as $(\langle \overline{u}_{\mathrm{surface}} \rangle - \langle \overline{u}_1 \rangle)/u_\tau$, where $\overline{u}_{\mathrm{surface}}$ is downwind velocity $\overline{u}_1$ evaluated at the surface. It is well known that the mean downwind velocity deficit under a shear-driven air–water interface exhibits behavior similar to the law of the wall in wall-bounded boundary layers. This is the case for the flow without LC, for which the mean downwind velocity deficit is characterized by a well-developed log law (Fig. 9b).

As can be seen in Fig. 9b, in flows with LC, the log-law profile of the velocity deficit is disrupted or eroded. This can be attributed in part to increased mixing induced by intensification of near-surface, small-scale eddies relative to the flow without LC (seen in Fig. 8). As noted earlier, this intensification of near-surface, small-scale eddies is associated with near-surface Stokes drift shear. For example, in Fig. 9b, comparing the case with $\mathrm{La}_t = 0.7$ and $\lambda = 6H$ to the case with $\mathrm{La}_t = 0.7$ and $\lambda = 4H/3$, it is seen that a decrease in λ while holding La_t fixed leads to a more pronounced disruption of the log law. The smaller value of λ serves to increase Stokes drift shear near the surface (see Fig. 2b), leading to higher levels of mixing near the surface caused by intensified small-scale eddies (see Figs. 8b,c) and thus greater disruption of the surface log law. A decrease in La_t can also lead to higher Stokes drift shear near the surface and thus

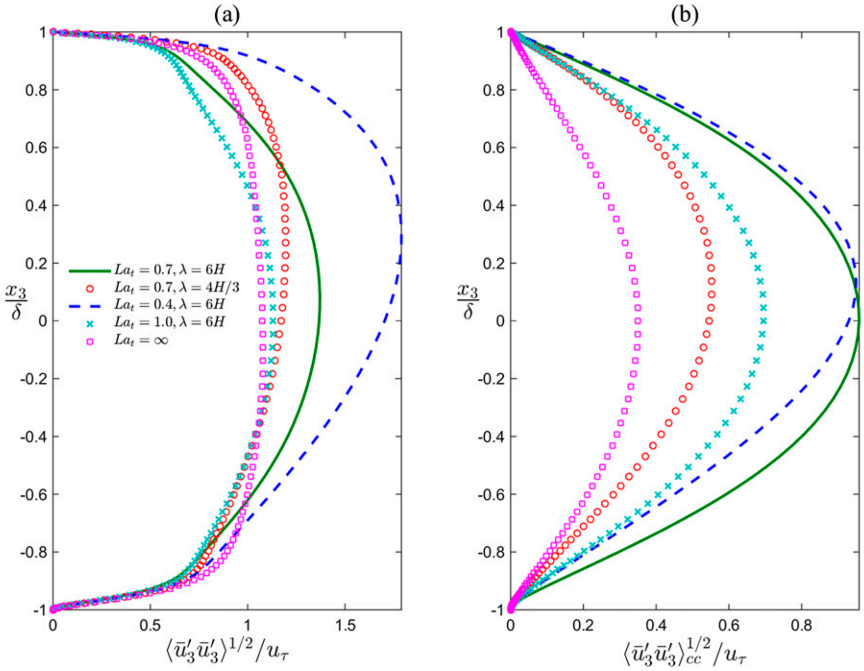

FIG. 7. (a) The rms of resolved vertical velocity and (b) contribution to resolved vertical velocity rms from full-depth LC.

greater disruption of the surface velocity log law, as can been seen comparing the case with $\mathrm{La}_t = 0.7$ and $\lambda = 6H$ to the case with $\mathrm{La}_t = 0.4$ and $\lambda = 6H$ (see Figs. 9b and 2b).

The impact of increasing Stokes drift shear on mean velocity can also be seen in Fig. 9a, showing a zoomed-in view of the near-surface velocity in regular units. Here it can be seen that the flows with LC with greatest near-surface Stokes drift shear [cases with ($\mathrm{La}_t = 0.4$, $\lambda = 6H$) and ($\mathrm{La}_t = 0.7$, $\lambda = 4H/3$), respectively] are characterized by thinner velocity boundary layers at the surface.

Recall that in flows without ($\mathrm{La}_t = 0.7$, $\lambda = 6H$), Stokes drift shear did not serve to enhance near-surface small eddies relative to the flow without LC. Thus, in the case with ($\mathrm{La}_t = 0.7$, $\lambda = 6H$) the disruption of the surface log law seen in Fig. 9b is attributed to Langmuir turbulence and associated LC.

2) DISRUPTION OF THE BOTTOM LOG LAW

The homogenizing action of LC induces a near-constant mean downwind velocity profile over the bulk region of the flow (see Fig. 10a). Furthermore, this homogenizing action extends deeper into the water column as the wavelength of the surface waves generating LC becomes larger (i.e., as λ becomes larger). This is expected based on the strength of full-depth LC, as described in the previous section in terms of crosswind and vertical velocity fluctuations (see, e.g., Fig. 6), and the form of the Stokes drift velocity shear in Fig. 2b,which has a depth-decay rate inversely proportional to λ.

Figure 10b shows mean velocity in wall units for flows with and without LC in the lower half of the water column. The full vertical axis in this figure extends from $x_3^+ \approx 0$ (denoting the bottom wall) up to $x_3^+ = 790$ (denoting the surface). To facilitate discussion of results, we have zoomed into the bottom log-layer region, showing only the part extending from $x_3^+ = 40$ up to $x_3^+ = 395$ (the middle of the water column). In the region below the bottom log layer that is not shown ($0 < x_3^+ < 40$), the velocity profiles for all cases are identical while satisfying the expected $u_1^+ = x_3^+$ theoretical profile within the viscous sublayer in the range $x_3^+ < 7$.

As seen in Fig. 10b, the flow without LC ($\mathrm{La}_t = \infty$) is characterized by a well-developed mean velocity log law in the bottom half of the water column. In the flow without LC, the log law extends from $x_3^+ \approx 50$ up to $x_3^+ \approx 200$. In the flow with LC generated by deep-water waves with $\lambda = 4H/3$, the mean velocity profile possesses a slight deviation from the log law. In the case of flows with LC generated by longer (intermediate) waves ($\lambda = 6H$), the effect of LC extends deeper into the water column, causing a larger deviation or erosion of the classical log law down to $x_3^+ \approx 90$ and

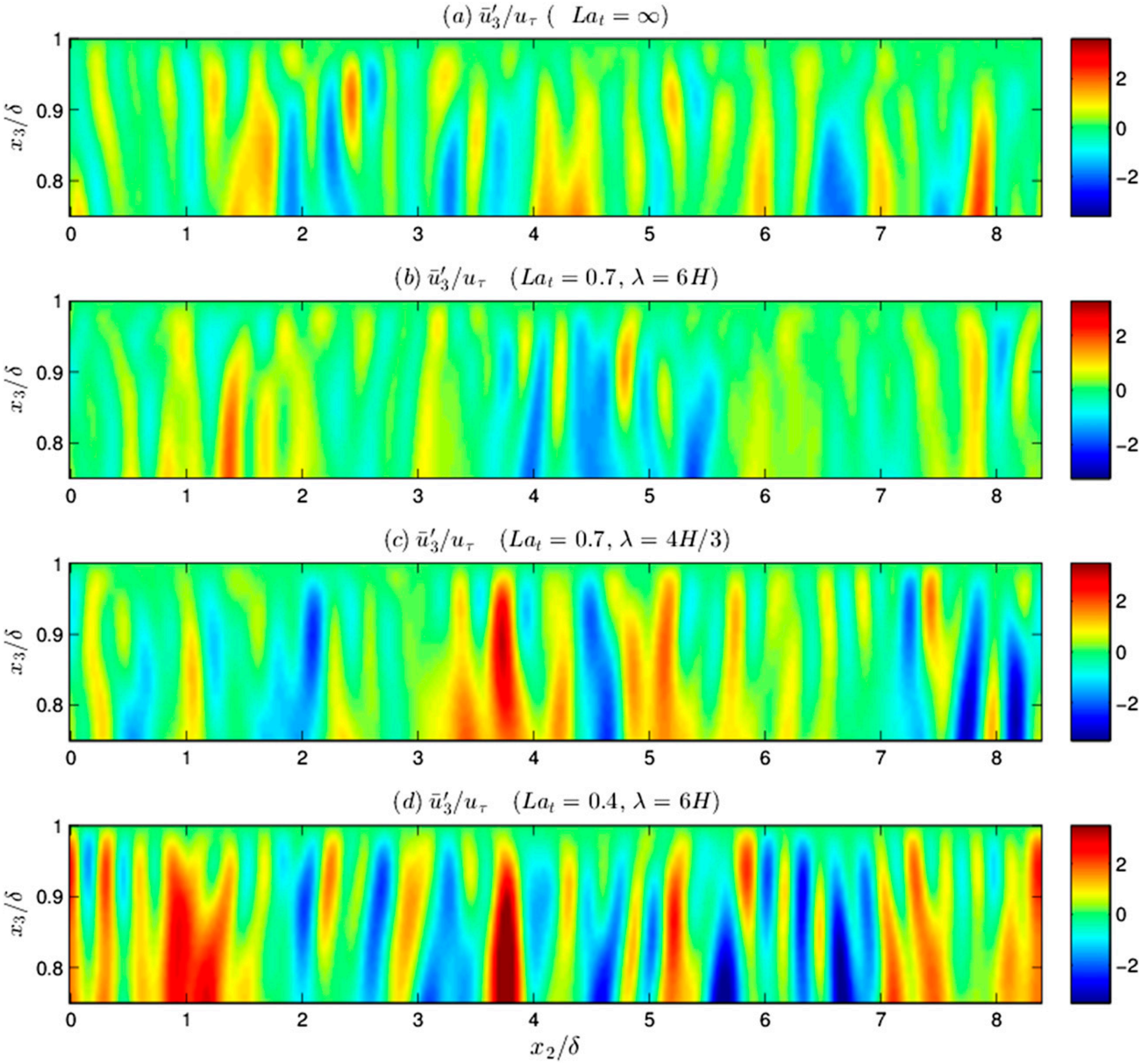

FIG. 8. Instantaneous snapshots of vertical velocity fluctuations at $x_1 = L_1/2$, where L_1 is the downwind length of the computational domain. These panels show the near-surface region extending from $x_3/\delta = 0.75$ through $x_3/\delta = 1$ (i.e., the upper one-eighth of the water column). Recall that the bottom of the water column is located at $x_3/\delta = -1$ and the surface is at $x_3/\delta = 1$. These panels highlight the downwellng and upwelling limbs of small-scale vortices near the surface.

inducing a velocity profile closer to the law of the wake (Pope 2000). This erosion is primarily caused by the downwelling limbs of the full-depth cells that bring well-mixed, high momentum closer to the bottom, resulting in a shift from a well-developed log law to a near constant profile for $x_3^+ > 100$, as seen in Figs. 11b–d.

In Fig. 10b, it can be seen that in the cases with $\lambda = 6H$, the case with $\mathrm{La}_t = 0.7$ is characterized by a more pronounced deviation from the log law compared to the case with $\mathrm{La}_t = 0.4$. The reason for this can be traced to the stronger upwelling limb of the $\mathrm{La}_t = 0.4$ case, observed by comparing Figs. 5b and 5e. This stronger upwelling limb brings slower-moving fluid to the log region (see Figs. 11b,c), serving to dampen the log-layer disrupting effect of the downwelling limb when averaging velocity over the crosswind direction (spanning both upwelling and downwelling limbs). Overall, this suggests a weaker full-depth LC in the lower half of the water column in the case with ($\mathrm{La}_t = 0.4$, $\lambda = 6H$) compared with the ($\mathrm{La}_t = 0.7$, $\lambda = 6H$) case, consistent with the earlier analysis of Figs. 5 and 7b.

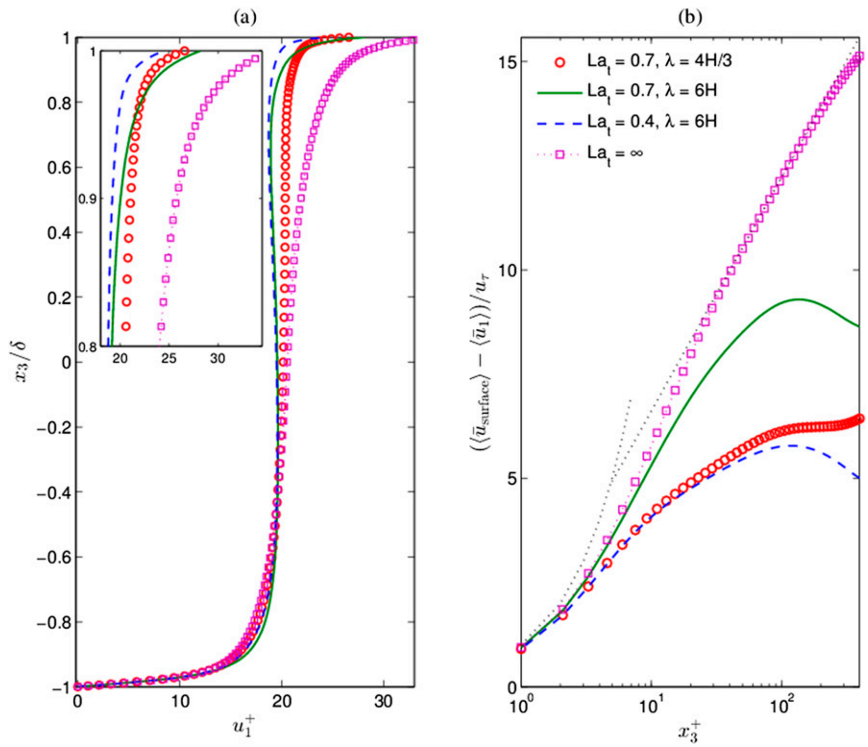

FIG. 9. (a) Mean downwind velocity and (b) mean downwind velocity deficit in the upper half of the water column in flows with and without LC; x_3^+ measures the distance to the surface in wall units.

c. *Reynolds shear stress and implications for its parameterization*

1) REYNOLDS SHEAR STRESS

The importance of full-depth LC in the generation of Reynolds shear stress $-\langle \overline{u}_1' \overline{u}_3' \rangle$ (the dominant Reynolds shear stress component for all flows studied here) can be seen, for example, in Fig. 4, where the full-depth dowelling limb of the cell generally coincides with a full-depth region of positive downwind velocity fluctuations and vice versa, contributing toward $-\langle \overline{u}_1' \overline{u}_3' \rangle > 0$. This contribution can be measured through the quantity

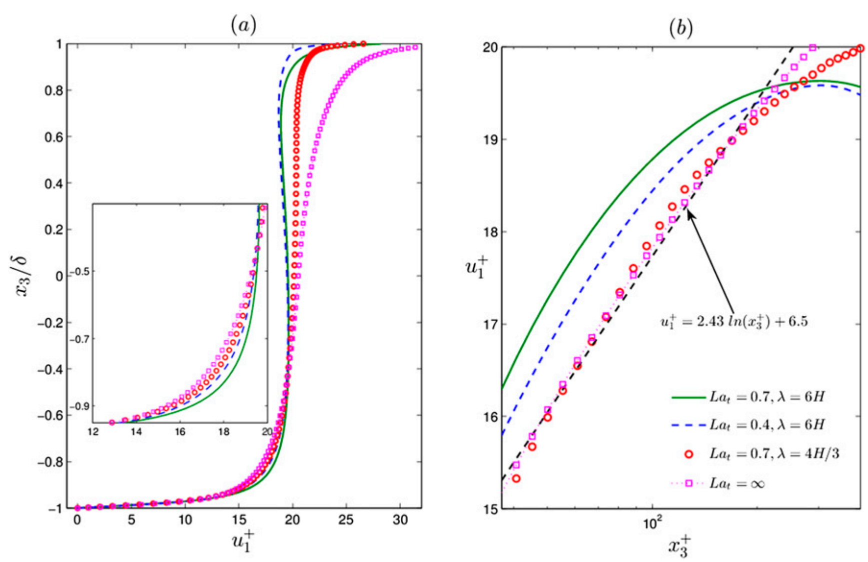

FIG. 10. As in Fig. 9, but for the lower half of the water column.

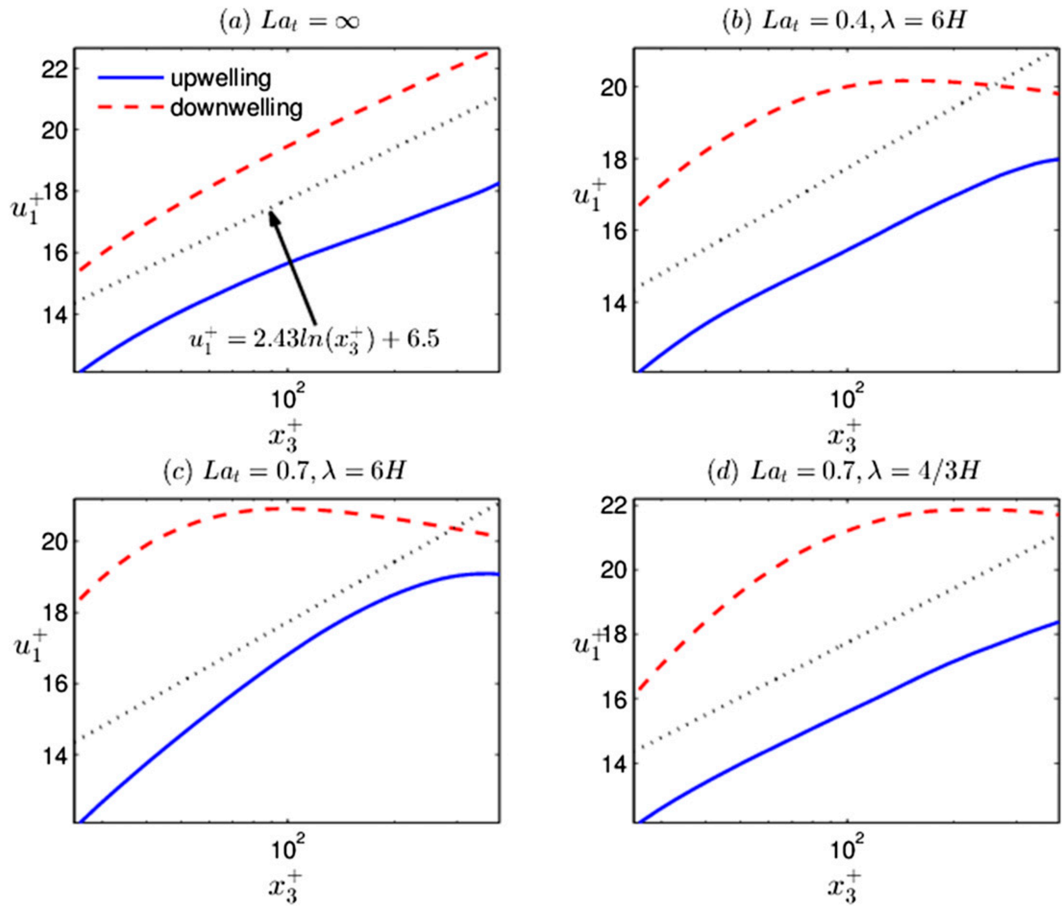

FIG. 11. Mean velocity profiles within downwelling and upwelling limbs of (a) Couette cells and (b)–(d) full-depth LCs.

$\langle \overline{u}_1' \overline{u}_3' \rangle_{\mathrm{CC}} = \langle \langle \overline{u}_1' \rangle_{t,x_1} \langle \overline{u}_3' \rangle_{t,x_1} \rangle$, obtained in a similar fashion to Eq. (6). In Fig. 12 it can be seen that $-\langle \overline{u}_1' \overline{u}_3' \rangle_{\mathrm{CC}}$ is a significant portion of the overall Reynolds shear stress.

Coherent cells such as full-depth LC act as a nonlocal source for turbulent vertical momentum flux [i.e., $\langle \overline{u}_1' \overline{u}_3' \rangle$; Kukulka et al. 2012; Smyth et al. 2002). Furthermore, as a result of the significant contribution toward Reynolds shear stress (RSS) from full-depth LC, especially in the interior of the water column as seen in Fig. 12, nonlocal transport induced by LC is expected to play an important role in the budgets of RSS.

2) RSS BUDGETS

Figure 13 shows budgets of the Reynolds shear stress $-\langle \overline{u}_1' \overline{u}_3' \rangle$. These budget terms are defined in appendix A. Within the surface log layer within the region $50 < x_3^+ < 100$ in the flow without LC (not shown), the only source is production by mean velocity shear. In flows with LC (shown in Fig. 13), production by mean velocity shear is a secondary source to production by Stokes drift shear. In flows with LC, within $50 < x_3^+ < 100$, production by mean velocity shear is significant; however, this production diminishes at depths $x_3^+ > 100$ below the surface. In some of the LC cases [e.g., the cases with ($\mathrm{La}_t = 0.7$, $\lambda = 6H$), ($\mathrm{La}_t = 0.4$, $\lambda = 6H$), and ($\mathrm{La}_t = 1.0$, $\lambda = 6H$)] the mean shear source switches signs, becoming a sink at depths below the $100 \leq x_3^+ \leq 150$ range. In Fig. 14, in the upper-half interior of the water column, it can be seen that for the cases with Langmuir turbulence in which production by mean shear becomes negative [i.e., the cases with ($\mathrm{La}_t = 0.7, \lambda = 6H$) and ($\mathrm{La}_t = 0.4, \lambda = 6H$)], turbulent transport (a nonlocal source) becomes an important component in balancing the destruction by mean shear. Furthermore, in these cases, turbulent transport [and pressure transport for the case with ($\mathrm{La}_t = 0.7, \lambda = 6H$)] and Stokes drift shear production are the sole sources. For example, in the ($\mathrm{La}_t = 0.7, \lambda = 6H$) case, turbulent transport attains a magnitude close to the magnitude of Stokes drift production for $x_3^+ > 300$. The trend of turbulent transport becoming more significant as a source helping to compensate for mean velocity shear becoming a greater sink can be seen in Fig. 15 for all of the flows with LC simulated.

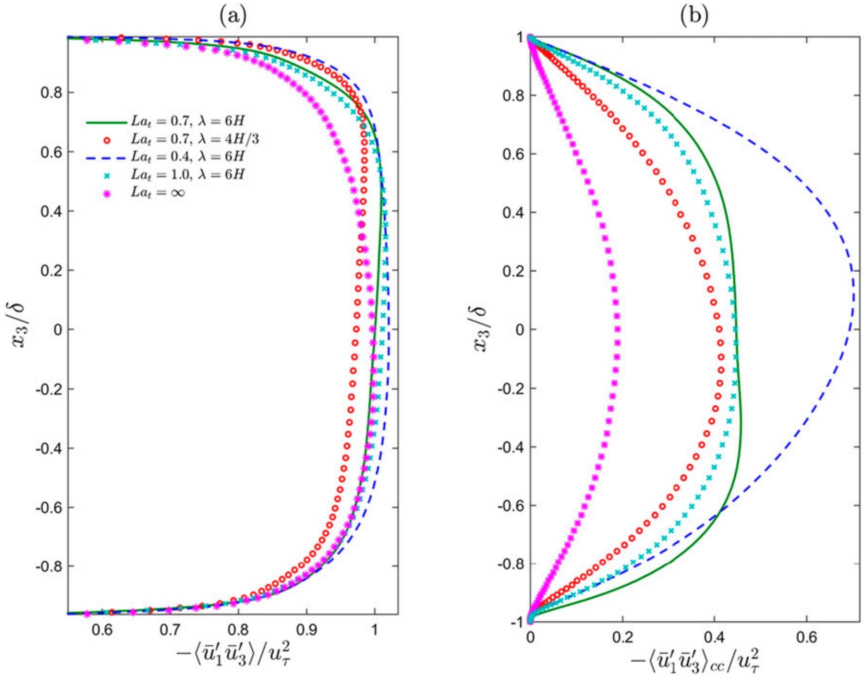

FIG. 12. (a) Resolved RSS and (b) contribution to resolved RSS from full-depth LCs.

The previous results indicate that a parameterization of the Reynolds shear stress should contain a nonlocal component and a local term based on the Stokes drift shear, in addition to the usual local term based on the vertical gradient of mean velocity. Furthermore, based on previous results, the nonlocal term is deemed necessary in order for the parameterization to be able to lead to negative velocity shear under certain combinations of wind and wave forcing parameters (La_t, λ).

From the RSS budget terms plotted in the upper half of the interior of the water column in Fig. 14, it can be seen that destruction of RSS by negative mean velocity shear occurs when the combination of local production by Stokes drift shear (ST) and turbulent (nonlocal) transport (T) is sufficiently large within this region of the water column. A proxy for the strength of the combined ST + T source can be taken to be the strength of full-depth LC in the upper half of the water column measured through $\langle \overline{u}'_3 \overline{u}'_3 \rangle_{\mathrm{CC}}^{1/2}$, as described earlier through Fig. 7b. For example, in Fig. 14, it can be seen that in flows with ($\mathrm{La}_t = 1.0$, $\lambda = 6H$), the source ST + T is not as great as it is for the cases with stronger full-depth LC (in this region) with ($\mathrm{La}_t = 0.7$, $\lambda = 6H$) and ($\mathrm{La}_t = 0.4$, $\lambda = 6H$). In the flow with ($\mathrm{La}_t = 0.7$, $\lambda = 4H/3$), the full-depth cells are weaker than in the other flows with LC and, correspondingly, the ST + T source is less than in the other flows. The previous information [on how the strength of full-depth LC can serve as a proxy for the (ST + T) source in the upper-half interior of the water column] will prove useful for calibrating one of the coefficients in the proposed Reynolds shear stress parameterization presented further below.

3) RSS PARAMETERIZATION VIA EDDY VISCOSITY

Figure 16b shows that the Reynolds shear stress is greater or equal to zero throughout the entire water column despite the negative mean velocity shear induced by Langmuir turbulence in some of the flows with LC (Fig. 16a) at depths below the surface. This suggests a breakdown of Reynolds-averaged Navier–Stokes (RANS) turbulence models, which for the wind-driven shear flows being considered here would model the Reynolds shear stress $-\langle \overline{u}'_1 \overline{u}'_3 \rangle$ as

$$-\langle \overline{u}'_1 \overline{u}'_3 \rangle = \nu_t^{\mathrm{RANS}} \frac{d\langle u_1 \rangle}{dx_3}, \tag{7}$$

where ν_t^{RANS} is an eddy viscosity. As previously determined through the RSS budgets in Figs. 13 and 15, a Reynolds shear stress model accounting for Langmuir turbulence should also include a local term proportional to Stokes drift shear because of its leading contribution to the production of $-\langle \overline{u}'_1 \overline{u}'_3 \rangle$. Furthermore, such a model should also contain a nonlocal term (i.e., a term not proportional to local velocity gradients) based on the significant contribution by turbulent transport as a source to the Reynolds shear stress budgets in cases when mean velocity shear becomes negative in the interior of the

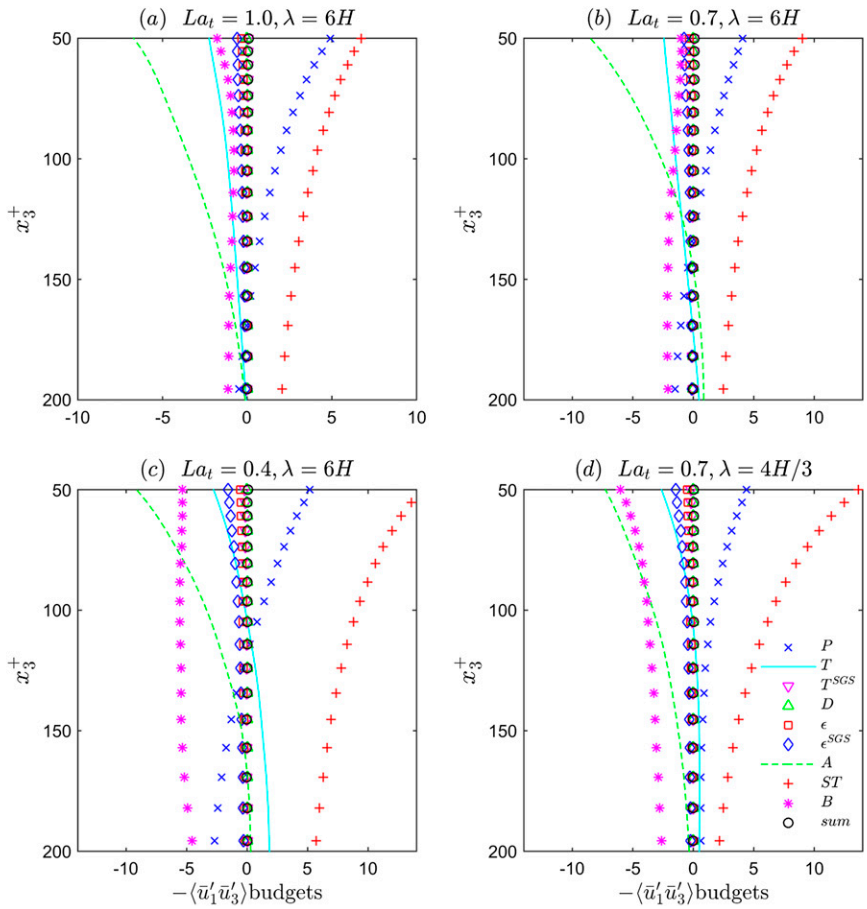

FIG. 13. Budget terms of $-\langle \overline{u}_1' \overline{u}_3' \rangle$ (scaled by u_τ^2) in flows with and without LC near the surface of the water column. Term x_3^+ measures distance from the surface in wall units, P is production by mean velocity shear, T is turbulent transport, T^{SGS} is SGS transport, D is viscous diffusion, ε is viscous dissipation, $\varepsilon^{\mathrm{SGS}}$ is SGS dissipation, A is pressure transport, ST is production by Stokes drift shear, and B is pressure–strain correlation.

water column. The local term proportional to Stokes drift shear and the nonlocal term together should overcome the negative flux induced by the local term proportional to mean velocity shear on the right-hand side of Eq. (7) and thus should lead to a positive Reynolds shear stress throughout the entire water column as expected from Fig. 16b. This balance is analogous to the partial balance between destruction of RSS by mean velocity shear (sink), local production by Stokes drift shear (source) and turbulent (nonlocal) transport (source), as seen previously in the RSS budget terms.

Although Langmuir turbulence can induce negative mean velocity shear throughout the core region of the water column, near the surface (approximately in the uppermost one-eighth of the water column), mean velocity shear is positive for all cases with LC, and thus the ansatz in Eq. (7) holds in this region without the need to add a local term proportional to Stokes drift shear nor a nonlocal term. As noted earlier, in this region, in cases with LC, Stokes drift shear can serve to enhance near-surface, small-scale eddies (see Fig. 8), ultimately leading to greater near-surface mixing. This is reflected by the near-surface rms of vertical velocity in Fig. 7a. This is also reflected through the Reynolds shear stress profiles shown in Fig. 16b. For example, in the upper one-eighth portion of the water column, the Reynolds shear stresses in flows with ($\mathrm{La}_t = 0.4$, $\lambda = 6H$) and ($\mathrm{La}_t = 0.7$, $\lambda = 4H/3$) are greater than in the other flows with LC characterized by lesser near-surface Stokes drift shear. This behavior is similar to the behavior of the rms of vertical velocity seen earlier in Fig. 10a and suggests an amplified RANS eddy viscosity near the surface.

The need for an enhanced near-surface eddy viscosity can be confirmed a posteriori based on LES fields. The eddy viscosity is computed by dividing the LES-resolved Reynolds shear stress by the LES mean velocity shear:

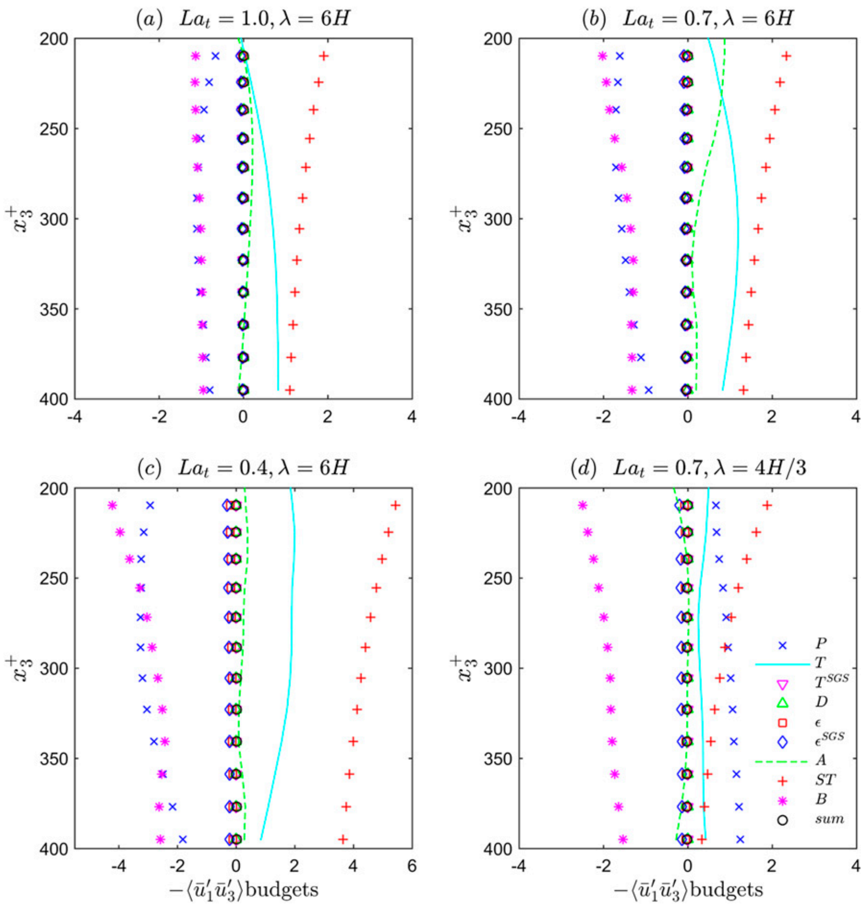

FIG. 14. As in Fig. 13, but in the upper-half interior of the water column.

$$\nu_t^{\mathrm{RANS}} = -\langle \overline{u}_1' \overline{u}_3' \rangle \Big/ \frac{d\langle \overline{u}_1 \rangle}{dx_3}\,. \tag{8}$$

The predicted eddy viscosities for all flows studied are shown in Fig. 17. As expected, the highest near-surface eddy viscosities correspond to the flows with the highest near-surface Stokes drift shear, that is, the flows with ($\mathrm{La}_t = 0.4$, $\lambda = 6H$) and ($\mathrm{La}_t = 0.7$, $\lambda = 4H/3$), respectively (see Fig. 2b). For a fixed value of La_t, a decrease in La_t (λ) leads to an increase in near-surface eddy viscosity, consistent with the trend in near-surface Stokes drift shear in Fig. 2b.

4) Enhanced near-surface eddy viscosity

To obtain an enhanced near-surface eddy viscosity to account for Stokes drift shear-enhanced, near-surface mixing in the KPP model, we proceed following Teixeira (2012). Analyzing the budget terms of Reynolds shear stress $-\langle \overline{u}_1' \overline{u}_3' \rangle$ shown in appendix A (in dimensionless form), it can be seen that (in dimensional form) production by mean wind-driven current velocity shear is $\langle u_3'^2 \rangle d\langle u_1 \rangle / dx_3$ while production by Stokes drift shear is $\langle u_1'^2 \rangle d\langle U_S \rangle / dx_3$, where U_S is the depth-dependent Stokes drift velocity, and where $U_S = \omega k a^2 U_1^s$. In an effort to find the influence of Langmuir turbulence on turbulent kinetic energy dissipation rate in the upper ocean, Teixeira (2012) decomposes the RSS as

$$-\langle u_1' u_3' \rangle = -\langle u_1' u_3' \rangle_{\mathrm{wind}} - \langle u_1' u_3' \rangle_{\mathrm{Stokes}}\,, \tag{9}$$

where the first term on the right-hand side is a component due to the wind-driven shear and the second term is a component due to the Stokes drift shear. In Eq. (9) nonlocal sources of RSS are neglected, consistent with the near-surface region $50 < x_3^+ < 100$ of the RSS budgets in Fig. 13. Furthermore, assuming a constant shear stress layer at the surface (Pope 2000), the total Reynolds shear stress can be taken as

$$-\langle u_1' u_3' \rangle = u_{\tau w}^2 \tag{10}$$

within the usual surface log layer, where $u_{\tau w}$ is wind stress friction velocity. Note that for the flows considered here, integration of the Reynolds-averaged

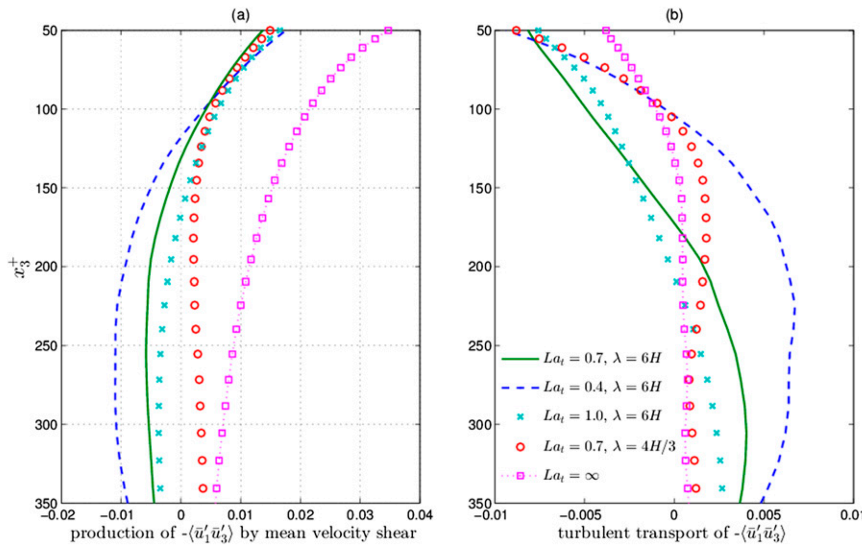

FIG. 15. (a) Production by mean velocity shear and (b) turbulent transport budget terms of $-\langle \overline{u}_1' \overline{u}_3' \rangle$ (scaled by u_τ^2) in flows with and without LC. Term x_3^+ measures distance to the surface in wall units.

downwind (streamwise) momentum equation yields $\nu d\langle u_1 \rangle / dx_3 - \langle u_1' u_3' \rangle = u_{\tau w}^2$ throughout the entire water column, where the first term on the left-hand side is the molecular viscous shear stress. Thus, the approximation in Eq. (10) neglects molecular viscous effects, which is valid within the surface log layer where mean velocity shear is relatively small compared to locations closer to the surface. The decomposition in Eq. (9) and the constant shear stress layer approximation in Eq. (10) suggest that $-\langle u_1' u_3' \rangle_{\mathrm{wind}} < u_{\tau w}^2$. This, along with the assumption that within the usual log layer the primary sources of RSS are wind-driven shear production and Stokes drift shear production (nonlocal sources are negligible), leads to the following expression of Teixeira (2012):

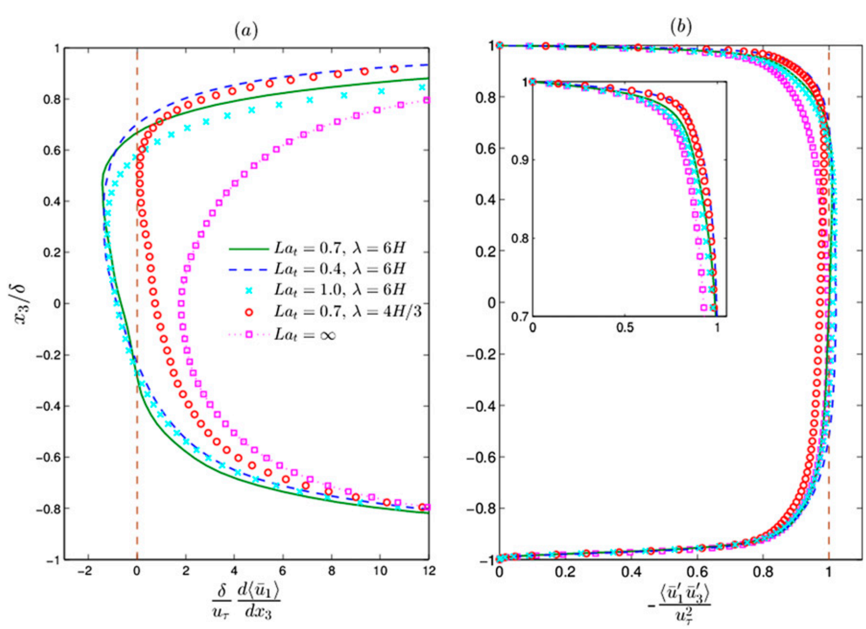

FIG. 16. (a) Mean velocity in the upper half of water column and (b) RSS $(-\langle \overline{u}_1' \overline{u}_3' \rangle)$ in flows with and without LC.

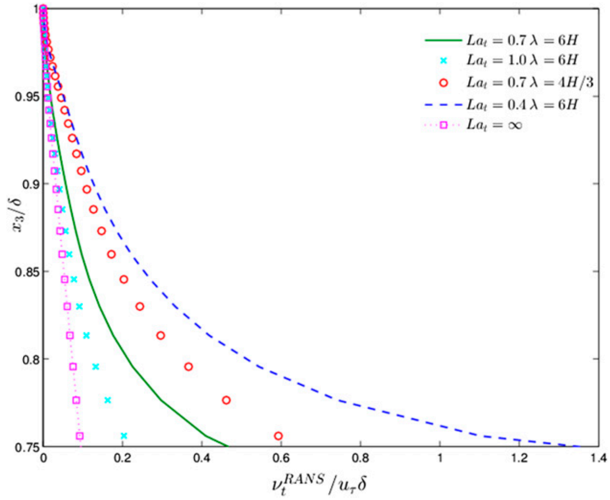

FIG. 17. A posteriori evaluation of the RANS eddy viscosity in the upper one-eighth portion of the water column based on LES fields.

$$-\langle u_1' u_3' \rangle_{\text{wind}} = \frac{u_{\tau w}^2}{1 + \dfrac{\langle u_1'^2 \rangle d\langle U_S \rangle}{\langle u_3'^2 \rangle dx_3} \Big/ \dfrac{d\langle u_1 \rangle}{dx_3}}. \tag{11}$$

The time scale

$$\gamma = \frac{\langle u_1'^2 \rangle}{\langle u_3'^2 \rangle d\langle u_1 \rangle / dx_3} \tag{12}$$

appearing in Eq. (11) may be parameterized via LES, as will be discussed further below.

The wind-driven shear component of the total RSS is modeled as

$$-\langle u_1' u_3' \rangle_{\text{wind}} = \nu_t \frac{d\langle u_1 \rangle}{dx_3}, \tag{13}$$

with the eddy viscosity within the surface log layer taken as $\nu_t = \kappa u_{\tau w} z$ (with z being distance to the surface). Note that in the eddy viscosity in Eq. (13), the superscript RANS [used earlier in Eq. (8)] has been dropped for ease of notation. Equating Eqs. (11) and (13) and making use of Eq. (12) leads to

$$\nu_t \left(1 + \gamma \frac{dU_S}{dx_3}\right) \frac{d\langle u_1 \rangle}{dx_3} = u_{\tau w}^2, \tag{14}$$

implying an amplified near-surface eddy viscosity with amplification factor $(1 + \gamma dU_S/dx_3)$. More specifically, equating Eqs. (10) and (14), it is seen that, for the total RSS in Eq. (9) with amplified eddy viscosity,

$$-\langle \overline{u}_1' \overline{u}_3' \rangle = \nu_t' \frac{d\langle u_1 \rangle}{dx_3} \tag{15}$$

and

$$\nu_t' = \nu_t \left(1 + \gamma \frac{dU_S}{dx_3}\right). \tag{16}$$

This amplified eddy viscosity is consistent with LES results, showing that Stokes drift shear serves to enhance near-surface mixing. For example, see intensification of near-surface small-scale vortices in Fig. 8, enhanced near-surface $\langle \overline{u}_3' \overline{u}_3' \rangle$ and $-\langle \overline{u}_1' \overline{u}_3' \rangle$ in Figs. 7a and 16b, and enhanced surface log-law disruption and momentum mixing (Fig. 9) with increasing Stokes drift shear.

Next, we discuss parameterization of the time scale in Eq. (12) using LES results. Near-surface depth profiles of the dimensionless time scale $\gamma u_{\tau w}/\delta$ are plotted in Fig. 18. In this figure it can be seen that $\gamma u_{\tau w}/\delta$ possesses a wide range of values near the surface; thus, the question arises of how this result can be used to parameterize the time scale in Eq. (18). First, recall that Eq. (9), which together with Eq. (10) led to Eqs. (11) and (12), is valid in the near-surface region where nonlocal sources of Reynolds shear stress are negligible. Furthermore, recall that Eq. (10) is valid where the molecular viscous stress is negligible. Looking at mean shear in Fig. 16a and the Reynolds shear stress budgets in Fig. 13, the neighborhood around $x_3/\delta \approx 0.75$ ($x_3^+ \approx 100$) is precisely where both Eqs. (9) and (10) are valid. In this neighborhood, mean shear is positive and relatively small (Fig. 16a; thus molecular viscous effects are negligible) and nonlocal sources are also negligible (Fig. 13), all in accordance with Eqs. (9)–(12). Hence, the time scale can be set to its corresponding values at $x_3/\delta \approx 0.75$ in Fig. 18 for the different flows with LC. These values lie within the approximate range $0.5 < \gamma u_{\tau w}/\delta < 1$. In the single-water-column simulations performed in the upcoming sections with a newly proposed RSS model based on Eqs. (11) and (12), we varied the parameter $\gamma u_{\tau w}/\delta$ between 0.5 and 2.5 in flows with LC and did not obtain significant sensitivity in mean velocity predictions (not shown). In forthcoming sections, results with this model will be shown with $\gamma u_{\tau w}/\delta = 1$.

4. A K-profile parameterization

LES results presented in the previous section indicate that a Reynolds shear stress (RANS turbulence) model able to represent shallow-water Langmuir turbulence characterized by full-depth LC should include the following:

1) an enhanced eddy viscosity near the surface to account for intensification of near-surface, small-scale vertical mixing induced by Stokes drift shear;

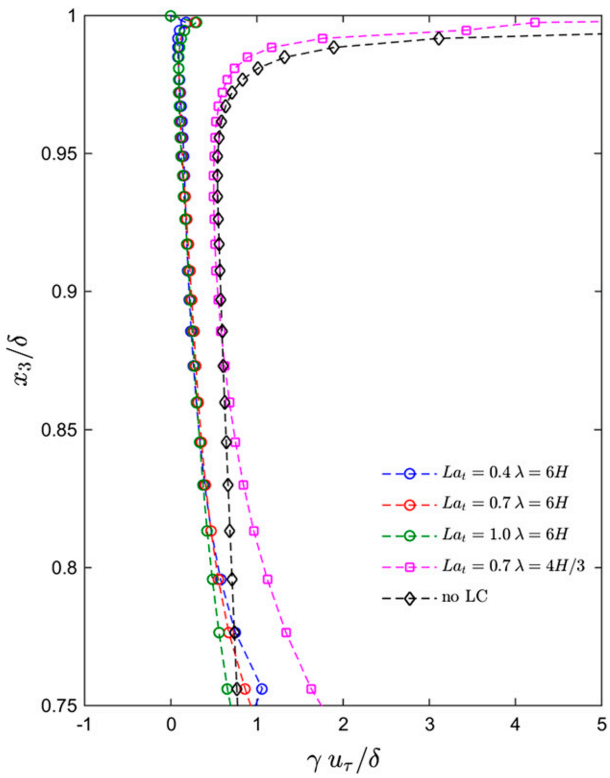

FIG. 18. Parameter γ in Eq. (18) evaluated using LES fields within the surface log layer.

2) a nonlocal flux accounting for the vertical transport induced by Langmuir turbulence coherent eddies; and
3) a local vertical flux down the gradient of Stokes drift velocity, as suggested by budgets of the RSS.

Next, a KPP model will be introduced possessing these characteristics.

a. A review of KPP

The RANS turbulence model developed is based on the K-profile parameterization reviewed by Large et al. (1994). The popularity of the KPP lies in its implementation simplicity given that it is an algebraic model unlike the Mellor–Yamada and k–ε models, which necessitate solutions of differential equations.

In the traditional KPP, the dominant component [i.e., the downwind (x_1)–wall-normal (x_3) component] of the Reynolds shear stress for the flows studied here (i.e., the flows with LC studied via LES) is modeled as

$$-\langle u_1' u_3' \rangle = \nu_t \frac{d\langle u_1 \rangle}{dx_3}. \tag{17}$$

Within the surface boundary layer the RANS eddy viscosity is taken as

$$\nu_t = \delta w(\sigma) G(\sigma), \tag{18}$$

where δ is the depth of the surface boundary layer, $w(\sigma)$ is a velocity scale, and $G(\sigma)$ is a shape function. In general, velocity scale w and shape function G are functions of σ, a dimensionless coordinate varying between 0 at the surface of the water column and 1 at the base of the surface boundary layer. In the present implementation [for the homogeneous (neutrally stratified) flows studied here] the surface boundary layer is taken to be the upper half of the water column. Dimensionless coordinate σ is defined as $\sigma = z/\delta$, where z measures the distance to the surface. Shape function G is taken to be a cubic polynomial:

$$G(\sigma) = a_0 + a_1\sigma + a_2\sigma^2 + a_3\sigma^3. \tag{19}$$

Velocity scale w and coefficients a_0 and a_1 are chosen so that the resulting eddy viscosity matches scale-similarity theory (i.e., log-layer dynamics; Pope 2000) near the surface. Velocity w is taken as $w = \kappa u_{\tau w}$, where $\kappa = 0.41$ is von Kármán's constant and $u_{\tau w}$ is wind stress friction velocity. Thus, w is independent of σ. Furthermore, $a_0 = 0$ and $a_1 = 1$. These two values together with $w = \kappa u_{\tau w}$ ensure that ν_t goes as $\kappa u_{\tau w} z$ within the surface log layer in accordance with similarity theory. In general, coefficients a_2 and a_3 are taken as

$$\begin{aligned} a_2 &= -2 + 3G(1) - \partial_\sigma G(1), \\ a_3 &= 1 - 2G(1) + \partial_\sigma G(1) \end{aligned} \tag{20}$$

with

$$\begin{aligned} G(1) &= \frac{\nu_{t0}}{\delta w(1)}, \\ \partial_\sigma G(1) &= \frac{\partial_z \nu_{t0}}{w(1)} - \frac{\nu_{t0}\partial_\sigma w(1)}{\delta w^2(1)} \end{aligned} \tag{21}$$

so as to allow for the eddy viscosity and its vertical derivative to match a prescribed interior eddy viscosity ν_{t0} and the latter's vertical derivative at the base of the surface layer (here corresponding to the middle of the water column; Large et al. 1994). Eddy viscosity ν_{t0} is obtained via an interior parameterization typically dependent on a Richardson number describing water column stability. For the homogenous flows considered here, ν_{t0} is independent of the Richardson number and is taken as a constant [thus, $\partial_z \nu_{t0} = 0$ in Eq. (21)]. In wind-driven flow without Langmuir cells, ν_{t0} is taken as the eddy viscosity at the middle of the water column predicted by the k–ε model. For flows with Langmuir forcing and thus full-depth LC, determination of the constant ν_{t0} will be described further below. As will be seen for these cases, ν_{t0} is an eddy viscosity associated with a nonlocal flux and a local flux down the gradient of Stokes drift shear, both associated with Langmuir turbulence. Finally, since ν_{t0} is a constant and in the standard KPP w is also taken as constant as ($w = \kappa u_{\tau w}$), the coefficients in Eq. (20) become

$$a_2 = -2 + 3\frac{\nu_{t0}}{\delta w},$$
$$a_3 = 1 - 2\frac{\nu_{t0}}{\delta w} \qquad (22)$$

for the standard KPP.

In the bottom half of the water column, within the bed log layer, the eddy viscosity is expected to behave similar to the surface log layer but as $\kappa u_{\tau b} z$, where $u_{\tau b}$ is bottom (bed) friction velocity and z is distance to the bottom wall. Shape function coefficients are also chosen so as to match the interior eddy viscosity ν_{t0}. Note that for the wind-driven flows considered here, in the mean $u_{\tau b} = u_{\tau w}$ (i.e., the mean wall shear stress is equal to the imposed wind stress). Thus, the shape function is symmetric about the middle of the water column.

b. Modification of KPP based on near-surface Langmuir turbulence dynamics

Recall that in the standard KPP, velocity scale w in Eq. (18) is taken independent of σ as $w = \kappa u_{\tau w}$, where $\kappa = 0.41$ is von Kármán's constant and $u_{\tau w}$ is wind stress friction velocity. The amplified eddy viscosity in Eq. (16) implies that the velocity scale should be

$$w' = \left(1 + \gamma \frac{dU_S}{dx_3}\right)\kappa u_{\tau w} \qquad (23)$$

for the modified KPP of the total Reynolds stress in Eq. (9). Thus, the amplified eddy viscosity may be calculated as in Eq. (18) but with w' given in Eq. (23):

$$\nu_t' = \delta w'(\sigma) G'(\sigma). \qquad (24)$$

Note that the new velocity scale w' affects the shape function coefficients calculated in Eq. (20), giving rise to a new shape function G'. More specifically, the new velocity scale is no longer constant and is now a function of σ through the depth dependence of the Stokes drift vertical shear, dU_S/dx_3. Thus, the shape function coefficients for the modified KPP are different than those for the standard KPP appearing in Eq. (22). The coefficients for shape function G' can be calculated from the general expressions in Eqs. (20) and (21) with w replaced by w', where w' is a function of σ unlike w. In the lower half of the water column, G' is taken as its mirror image from the upper half as is done in the case of G, and thus G' is symmetric about the middle of the water column. However, the resulting eddy viscosity in Eq. (24) is not symmetric about middepth given the depth decay of w' through the Stokes drift shear [see Eq. (23) and Fig. 2b]. In summary, the new KPP model is taken as the original KPP model, but with the amplified velocity scale given in Eq. (23). Note that McWilliams and Sullivan (2000) proposed an amplified velocity scale where the amplification is dependent on the turbulent Langmuir number La_t rather than on Stokes drift shear as is the LES-supported result from the analysis here.

c. Modification of KPP accounting for nonlocal transport and local Stokes drift shear production

As shown earlier through analysis of Reynolds shear stress budgets, the RSS model should account for turbulent (nonlocal) transport in the interior of the water column as well as local production by Stokes drift shear. We proceed similar to McWilliams and Sullivan (2000) and Smyth et al. (2002), who introduced a countergradient term into the KPP to account for nonlocal transport and Stokes drift shear production, both key mechanisms of Langmuir turbulence:

$$-\langle u_1' u_3' \rangle = \nu_t' \left(\frac{d\langle u_1 \rangle}{dx_3} + \Gamma\right), \qquad (25)$$

where Γ is a countergradient defined as

$$\Gamma = \frac{u_{\tau w}^2}{\nu(\sigma)\delta}, \qquad (26)$$

with $\nu(\sigma)$ as a velocity scale. Countergradients such as this one have been proposed for the nonlocal transport of scalars in the convective atmospheric boundary layer (see, e.g., Frech and Mahrt 1995, and references therein) and have been extended to the momentum equations for the upper-ocean mixed layer (see, e.g., Smyth et al. 2002). In the case of Smyth et al. (2002), the countergradient was augmented with Stokes drift shear to account for local production by the latter. In the present formulation this will not be needed, as the product $\nu_t'\Gamma$ in Eq. (25) inherently possesses such a term, as will be described further below.

In the current implementation, general velocity scale $\nu(\sigma)$ in Eq. (26) is taken independent of σ as simply $\kappa u_{\tau w}$. It is not taken as that given by Eq. (23) because the latter is not representative of core (bulk) region dynamics, but rather of Stokes drift shear-enhanced mixing in the near-surface region.

As per the discussion in the previous section, the KPP eddy viscosity is designed to match the eddy viscosity at the base of the surface layer (in this case ν_{t0}'). This eddy viscosity may be found by setting the countergradient term in Eq. (25) at the middle of the water column proportional to the wind stress:

$$\nu'_{t0}\Gamma = Cu^2_{\tau w}, \tag{27}$$

where C is indicative of the strength of Langmuir turbulence through nonlocal transport and local production by Stokes drift shear of RSS at middepth. Calibration of C will be demonstrated further below in the presentation of single-water-column model results with the modified KPP. As seen through the analysis of the RSS budgets in Fig. 14, the combined source of Stokes drift shear production (ST) and turbulent transport (T) can lead to negative mean velocity shear. Results with the single-water-column model will show that if wind and wave forcing conditions are such that the ST and T sources are sufficiently high to cause a negative mean velocity shear, then $C > 1$; otherwise, $C \le 1$. Furthermore, as originally described earlier in section 3c(2), looking at the RSS budget terms in Fig. 14, it can be seen that the combined ST and T source increases with strength of full-depth LC in the upper half of the water column as measured via $\langle \overline{u}'_3\overline{u}'_3\rangle^{1/2}_{\mathrm{CC}}$ in Fig. 7b. Recall that the quantity $\langle \overline{u}'_3\overline{u}'_3\rangle^{1/2}_{\mathrm{CC}}$ represents the contribution of full-depth LC to rms of vertical velocity, $\langle \overline{u}'_3\overline{u}'_3\rangle^{1/2}$. This presents a path for future parameterization of C.

FLUX DOWN THE STOKES DRIFT GRADIENT

Inserting Eq. (16) into Eq. (25) and expanding reveals that the modified KPP contains the term $(\nu_t\Gamma\gamma)dU_S/dx_3$. This represents a local term in the form of flux down the vertical gradient of Stokes drift. The RSS transport equation derived from the momentum equation with CL (Langmuir) forcing (serving to generate Langmuir turbulence) possesses local production by vertical gradients of mean downwind velocity and Stokes drift velocity, $d\langle u_1\rangle/dx_3$ and dU_S/dx_3, respectively. This, along with the LES-based analysis of RSS transport equation terms (i.e., the budget terms presented earlier), suggests that a parameterization of the RSS should contain a vertical flux down the gradient dU_S/dx_3, in addition to the usual flux down the gradient $d\langle u_1\rangle/dx_3$. Reynolds shear stress parameterizations, including transport down the gradient dU_S/dx_3, have been postulated by Harcourt (2013) and McWilliams et al. (2012) for Langmuir turbulence in the upper-ocean mixed layer. Note that Langmuir turbulence in the upper-ocean mixed layer possesses a number of differences from Langmuir turbulence in shallow water, primarily associated with the coherency of the full-depth LC in shallow water. In the shallow water case, full-depth LC tends to be strongly coherent, contributing greatly to turbulent (nonlocal) transport of RSS and disrupting the bottom log layer. In the upper ocean, the LCs are less coherent and do not interact with the bottom log layer.

5. Evaluation of the modified KPP

Single-water-column RANS simulations of wind-driven flows at $\mathrm{Re}_\tau = 395$ (based on wind stress friction velocity and water column middepth) with full-depth LC were performed with the standard KPP, the k–ε model, and the newly proposed modified KPP for various combinations of wind and wave forcing. LES results of these same flows were presented earlier. Recall that wind-driven flows with LC are characterized by the dominant wavelength of surface gravity waves (λ) generating LC and the turbulent Langmuir number (La_t), which is inversely proportional to the strength of wave forcing relative to wind forcing. Four cases have been simulated: ($\mathrm{La}_t = 0.7$, $\lambda = 6H$), ($\mathrm{La}_t = 0.4$, $\lambda = 6H$), ($\mathrm{La}_t = 1.0$, $\lambda = 6H$), and ($\mathrm{La}_t = 0.7$, $\lambda = 4H/3$).

RANS simulations consisted of solving the Reynolds-averaged continuity equation and momentum equation with CL vortex force solved using the ANSYS Fluent software tool (release 14.0; http://www.ansys.com/Products/Fluids/ANSYS+Fluent). [An alternate approach was developed (discussed in appendix B) and yielded similar results to Fluent.] The domain was chosen as in Fig. 1, but with two hexahedral elements in the downwind direction and two hexahedral elements in the crosswind direction. This coarse resolution in horizontal directions prevents resolution of Langmuir cells resulting in a single (1D) water column model. In the vertical direction, the domain was discretized with 33 equally distant points; thus, the first grid point away from the bottom (surface) was at a distance $z_1^+ = 25$ from the bottom (surface). As a result, these simulations do not resolve viscous nor buffer sublayers, and resolution only extends into the log layer. The surface boundary condition consists of a prescribed wind stress, the same as in the LES. The bottom boundary condition will be described in detail further below.

Figure 19 compares mean downwind velocity predicted by LES (described earlier) and by RANS with the modified KPP, standard KPP, and k–ε model. With respect to LES, the RANS with modified KPP leads to a better prediction than with standard KPP and k–ε model in representing 1) the mixing of momentum throughout the bulk flow region and at the bottom of the water column induced by Langmuir turbulence and associated full-depth LC and 2) the near-surface mixing induced by near-surface, small-scale vortices enhanced by Stokes drift shear. In some cases, the simulations with modified KPP tend to overpredict the near-surface mixing of

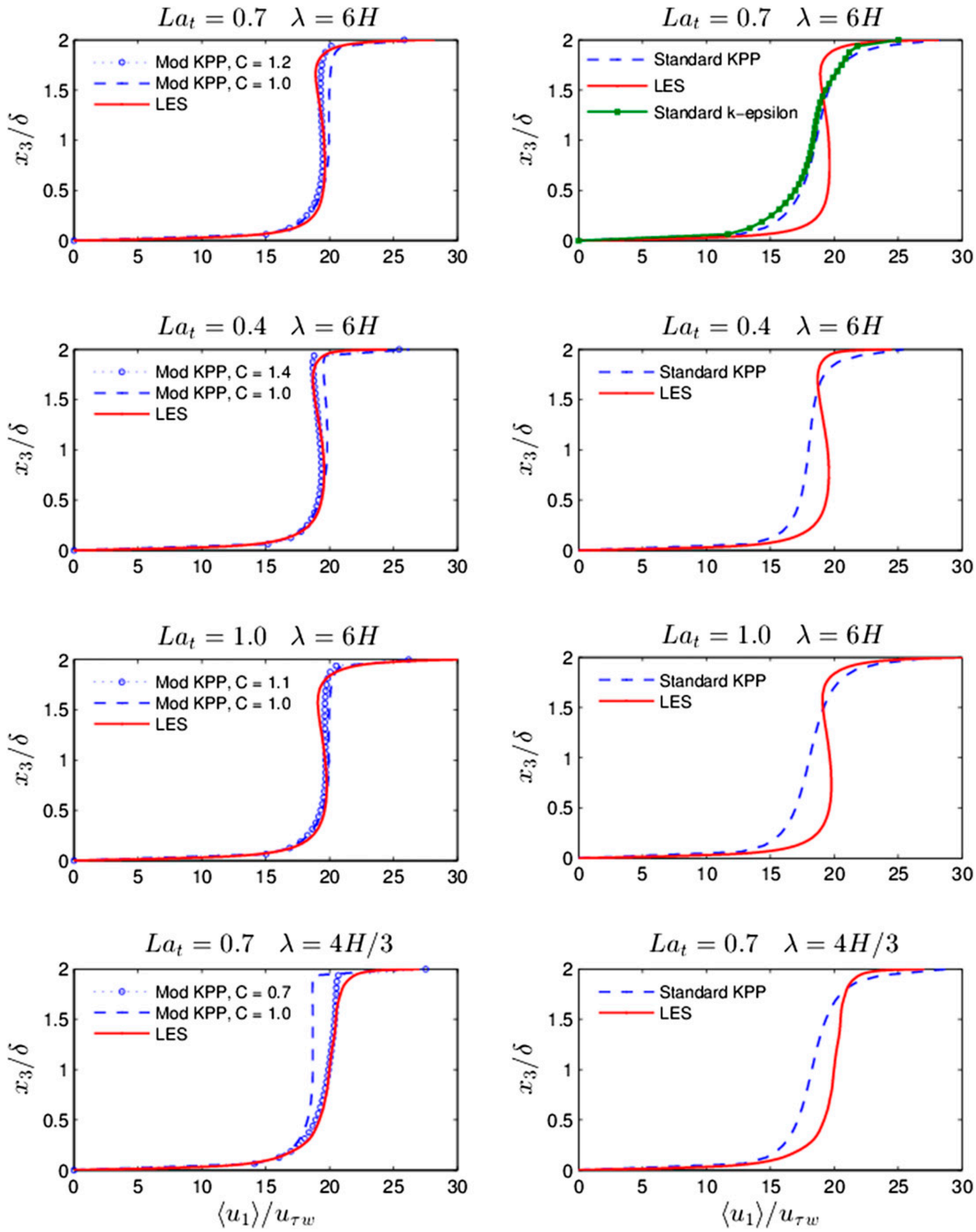

FIG. 19. Comparison between RANS and LES of flows with LC at $\mathrm{Re}_\tau = 395$. RANS is performed with the k–ε model, the standard KPP, and the modified KPP accounting for Langmuir turbulence and associated full-depth LC. Note that $H = 2\delta$ is the depth water column.

momentum, such as in the flow with ($\mathrm{La}_t = 0.7, \lambda = 4H/3$). This is attributed to the coarse mesh that only provides two grid points to resolve the rapid transition of the mean velocity at the surface.

Recall that the modified KPP coefficient C in Eq. (27) was said to be representative of the strength of the full-depth LC in the upper-half of the water column. From the results in Fig. 19, it can be concluded that the C coefficient is indeed dependent on the strength of full-depth LC in the upper-half of the water column as measured through $\langle \overline{u}_3' \overline{u}_3' \rangle_{\mathrm{CC}}^{1/2}$ (plotted in Fig. 7b for the various cases of LES with LC). More specifically,

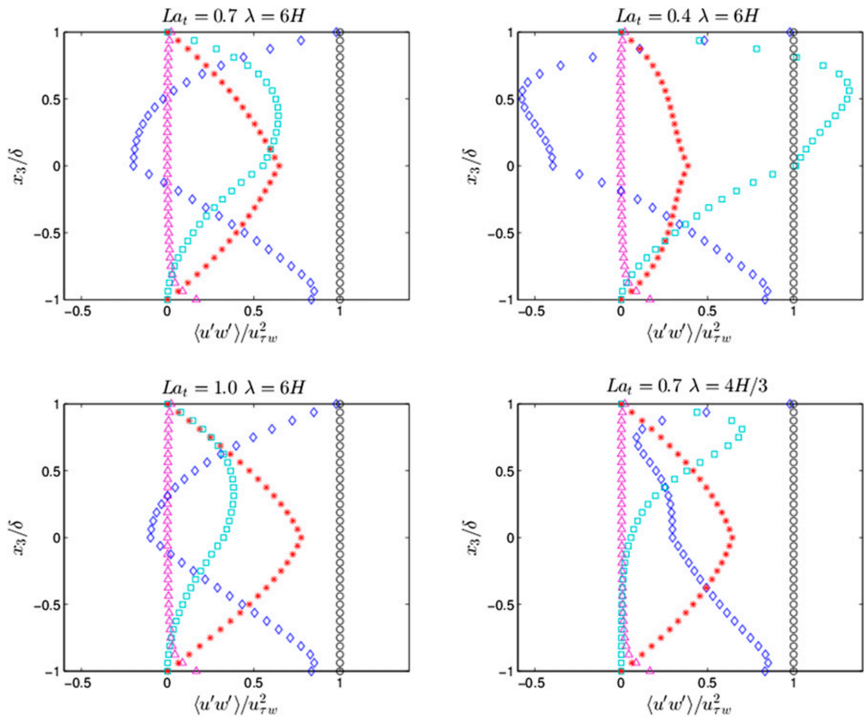

FIG. 20. Momentum balance for modified nonlocal KPP in flows with LC at $\mathrm{Re}_\tau = 395$. Red stars are nonlocal stress, pink triangles are local molecular viscous stress, purple diamonds are local eddy viscosity stress, aqua squares are flux down the gradient of Stokes drift velocity, and gray circles are sums.

Fig. 19 shows results with $C = 1$ and with tuned values of C so as to yield mean velocity profiles in closer agreement with the LES. The tuned values of C are consistent with the strength of full-depth LC in the upper-half of the water column evaluated through $\langle \overline{u}_3' \overline{u}_3' \rangle_{\mathrm{CC}}^{1/2}$: for ($\mathrm{La}_t = 0.4, \lambda = 6H$), $C = 1.4$; for ($\mathrm{La}_t = 0.7$, $\lambda = 6H$), $C = 1.2$; for ($\mathrm{La}_t = 1.0, \lambda = 6H$), $C = 1.1$; and for ($\mathrm{La}_t = 0.7, \lambda = 4H/3$), $C = 0.7$. Thus, as expected, a parameterization of the effect of a weaker full-depth LC in the upper-half of the water column via the modified KPP requires a smaller value of C. Future research should focus on obtaining a parameterization of C via strength of the full-depth LC (i.e., $\langle \overline{u}_3' \overline{u}_3' \rangle_{\mathrm{CC}}^{1/2}$) in the upper-half of the water column in terms of La_t and λ by performing a suite of LES simulations sweeping through a range of these parameters.

In addition to being dependent on the Reynolds shear stress model, the results of Fig. 19 are also strongly dependent on the bottom boundary condition of the simulations. The bottom boundary condition and its modification to account for log-law disruption caused by full-depth LC will be described in the detail in the upcoming subsection.

Figure 20 shows momentum balances in the RANS simulations of wind-driven flows with LC for the cases ($\mathrm{La}_t = 0.4$, $\lambda = 6H$) with $C = 1.4$, ($\mathrm{La}_t = 0.7$, $\lambda = 6H$) with $C = 1.2$, ($\mathrm{La}_t = 1, \lambda = 6H$) with $C = 1.1$, and ($\mathrm{La}_t = 0.7$, $\lambda = 4H/3$) with $C = 0.7$. The RANS equation governing these flows yield the following balance:

$$\nu \frac{d\langle u_1 \rangle}{dx_3} - \langle u_1' u_3' \rangle = u_{\tau w}^2, \tag{28}$$

where the first term on the left-hand side is the local molecular viscous stress. The RSS is modeled via the modified KPP in Eq. (25) [while using Eqs. (23) and (24)]:

$$-\langle u_1' u_3' \rangle = \nu_t' \frac{d\langle u_1 \rangle}{dx_3} + \eta\Gamma + \eta\Gamma\gamma \frac{dU_S}{dx_3}, \tag{29}$$

where $\eta = \delta\kappa u_{\tau w} G'(\sigma)$. The first term on the right-hand side is the local eddy viscosity stress or local flux down the gradient of mean velocity, the second term is the nonlocal flux, and the third term is the local flux down the gradient of Stokes drift. The latter was discussed earlier in section 4c. Figure 20 shows that the four stresses [local molecular viscosity stress, local eddy viscosity stress, nonlocal flux, and flux down the gradient of Stokes drift in Eqs. (28) and (29)] sum to the square of the wind stress friction velocity $u_{\tau w}^2$, as expected given Eq. (28).

Looking at Fig. 20, in flows where the contribution of the flux down the gradient of Stokes drift is lower [e.g., in the flow with ($La_t = 1.0, \lambda = 6H$)], the contribution of the nonlocal stress is higher and vice versa. For example, in the flow with ($La_t = 1.0, \lambda = 6H$), Stokes drift shear is smallest compared to the other flows, leading to a relatively small contribution from the flux down the gradient of Stokes drift in the modified KPP model. Furthermore, the presence of the full-depth LC in this case serves to homogenize the entire water column, leading to small contributions from the local stresses based on mean velocity shear, especially in the middle of the water column (which is expected given that these stresses are proportional to vertical gradient of mean downwind velocity). As a result, in the ($La_t = 1.0, \lambda = 6H$) case, the nonlocal stress is left to provide the bulk of wind shear stress vertical transfer throughout the water column, serving to explain why the nonlocal stress in this flow is higher than in the other cases.

Finally, note that in Fig. 20, in some of the flows it is seen that the local eddy viscosity stress becomes negative throughout significant portions of the water column [e.g., in the ($La_t = 1.0, \lambda = 6H$) case]. This is because of the negative vertical gradient of mean downwind velocity induced by Langmuir turbulence (through nonlocal transport and Stokes drift shear production mechanisms), consistent with the LES results presented earlier.

Bottom boundary condition

In the single-water-column RANS simulations previously described, the bottom boundary condition consists of a prescribed bottom stress. The reason for this is that sole imposition of the no-slip condition would require resolution of the buffer and viscous wall regions below the log-layer. To avoid resolution of these computationally expensive regions, the RANS simulation performed relies on imposition of the bottom stress in what is often referred to as near-wall modeling. The bottom stress is defined in terms of the bed stress friction velocity (which in these flows is equal to the wind stress friction velocity $u_{\tau w}$). In near-wall modeling (Pope 2000) the bed stress friction velocity is obtained by assuming that the computed mean velocity $\langle u_1 \rangle$ satisfies the log law at the first grid point away from the bottom wall:

$$\frac{\langle u_1 \rangle}{u_{\tau w}} = \frac{1}{\kappa} \ln\left(\frac{u_{\tau w} z}{\upsilon}\right) + B, \tag{30}$$

where $B = 5.5$ for classical boundary layers. In traditional near-wall modeling, the previous equation is solved dynamically (i.e., during the simulation) for $u_{\tau w}$, with z set equal to the distance between the wall and the first grid point away from the wall and $\langle u_1 \rangle$ set as the computed mean velocity at the first grid point away from the wall.

LES presented earlier has shown that full-depth LC disrupts the bottom log-law velocity profile in Eq. (30) (recall Fig. 10b). The behavior induced by the full-depth LC can be approximated by varying the value of B in Eq. (30) depending on the strength of full-depth LC in the lower half of the water column. For example, in flows with ($La_t = 0.7, \lambda = 6H$), the LES has shown that the disrupted log law caused by full-depth LC may be approximated by resetting B to 7.5 in the log law in Eq. (30) (not shown). In flows with ($La_t = 0.7, \lambda = 4H/3$) in which the full-depth LC is weaker and less disruptive in the lower half of the water column than in the ($La_t = 0.7, \lambda = 6H$) case, the LES has shown that the disrupted log law may be approximated by resetting B to 6.5. Thus, a more disruptive full-depth LC in the lower-half of the water column requires a higher value of B. Similar conclusions can be obtained by comparing the cases with ($La_t = 0.7, \lambda = 6H$) and ($La_t = 0.4, \lambda = 6H$). This indicates that B can be parameterized via the strength of full-depth LC (i.e., $\langle \overline{u}_3' \overline{u}_3' \rangle_{CC}^{1/2}$) in the lower half of the water column.

Figure 21 shows mean velocities obtained in RANS simulations with the modified KPP with different values of the B coefficient in the log law used for near-wall modeling. For example, in the flow with ($La_t = 0.7, \lambda = 6H$), the log law in Eq. (30) with $B = 7.5$ leads to a velocity profile in better approximation of the LES velocity profile than the traditional $B = 5.5$, as expected. The significant difference between using $B = 5.5$ and $B = 7.5$ in the RANS single-water-column simulation with modified KPP model can be seen in Fig. 21 in terms of bulk downwind momentum and log-layer disruption. The importance of the B coefficient in the near-wall model is further demonstrated in Fig. 21 for the flow with ($La_t = 0.7, \lambda = 4H/3$). Following the LES results and setting $B = 6.5$ in the near-wall model in the RANS simulation with modified KPP leads to a better result than $B = 5.5$.

6. Summary and conclusions

Langmuir turbulence is generated by interaction between Stokes drift velocity induced by surface gravity waves and the wind-driven shear. In homogeneous shallow water, Langmuir turbulence is often characterized by full-depth LC engulfing the entire water column. LES of Langmuir turbulence with full-depth LC in a wind-driven shear current has revealed that mixing due to full-depth LC erodes the bottom log-law velocity profile, inducing a

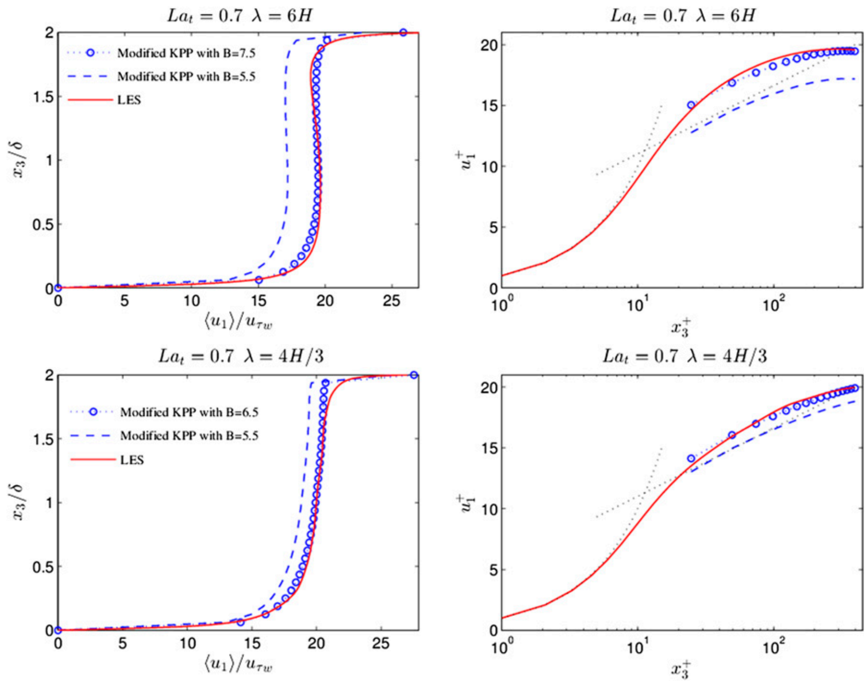

FIG. 21. Mean downwind velocity predicted in RANS with modified KPP and various different values of B coefficient in the log law used for near-wall modeling.

profile resembling a wake law. Turbulent (nonlocal) transport and local Stokes drift shear production sources of Reynolds shear stress in Langmuir turbulence induce negative mean velocity shear under certain combinations of wind and wave forcing parameters. Meanwhile, near the surface, Stokes drift shear serves to intensify small-scale eddies, leading to enhanced mixing and disruption of the surface velocity log law.

A K-profile parameterization (KPP) of the Reynolds shear stress composed of local and nonlocal components has been introduced capturing the previously summarized basic mechanisms by which Langmuir turbulence and associated full-depth LC impact the mean flow. Single-water-column RANS simulations with the new parameterization were presented showing good agreement with LES in terms of mean velocity profiles. The KPP introduced is characterized by two coefficients (C and B) dependent on the strength of the full-depth LC in the upper half of the water column and its strength in the bottom half of the water column. Future research should focus on parameterizing these coefficients as functions wind and wave forcing parameters λ and La_t by performing a suite of LES over likely values of these parameters. Alternatively, field measurements of full-depth LC such as those of Gargett and Wells (2007) could also be used to parameterize these coefficients. It is important to realize the significance/benefit of having linked these coefficients to the strength of full-depth LC, as, for example, the C coefficient had been originally tied to nonlocal transport in the Reynolds shear stress budgets, which might not be accessible through field measurements.

Acknowledgments. The authors are grateful for support from NSF Grants 0846510, 0927054, and 0927724. This research was also partially supported by a grant from BP/the Gulf of Mexico Research Initiative through the CARTHE-II consortium.

APPENDIX A

Reynolds Shear Stress Budget Terms

Following the Reynolds decomposition of the LES-resolved velocity $\overline{u}_i = \langle \overline{u} \rangle_i + \overline{u}_i'$ and expanding the pressure $\overline{\Pi}$ following its definition in Eq. (3), the transport equation for the Reynolds shear stress $-\langle \overline{u}_1' \overline{u}_3' \rangle$ for the flows considered in statistical equilibrium can be shown to reduce to

$$P_{13} + Q_{13} + T_{13} + T_{13}^{\mathrm{sgs}} + D_{13} + A_{13} + B_{13} + \varepsilon_{13} + \varepsilon_{13}^{\mathrm{sgs}} = 0, \tag{A1}$$

where

$$P_{13} = \langle \overline{u}_3' \overline{u}_3' \rangle \frac{d\langle \overline{u}_1 \rangle}{dx_3} \text{ (mean shear production rate)},$$

$$Q_{13}=\frac{1}{\mathrm{La}_t^2}\langle\overline{u}_1'\overline{u}_1'\rangle\frac{dU_1^S}{dx_3}\ \text{(Stokes drift shear production rate)},$$

$$T_{13}=-\frac{d\langle\overline{u}_1'\overline{u}_3'\overline{u}_3'\rangle}{dx_3}\ \text{(turbulent transport rate)},$$

$$T_{13}^{\mathrm{sgs}}=\frac{d\langle\overline{u}_3'\tau_{13}^{d'}\rangle}{dx_3}\ \text{(SGS transport rate)},$$

$$D_{13}=\frac{1}{\mathrm{Re}_\tau}\frac{d^2\langle\overline{u}_1'\overline{u}_3'\rangle}{dx_3^2}\ \text{(viscous diffusion rate)},$$

$$A_{13}=-\frac{d\langle\overline{P}'\overline{u}_1'\rangle}{dx_3}\ \text{(pressure transport rate)},$$

$$B_{13}=2\langle\overline{P}'\overline{S}_{13}'\rangle\ \text{(pressure-strain redistribution rate)},$$

$$\varepsilon_{13}=-\frac{2}{\mathrm{Re}_\tau}\frac{\partial\overline{u}_1'}{\partial x_3}\frac{\partial\overline{u}_3'}{\partial x_3}\ \text{(viscous dissipation rate), and}$$

$$\varepsilon_{13}^{\mathrm{sgs}}=-\tau_{13}^{d'}\frac{\partial\overline{u}_3'}{\partial x_3}-\tau_{33}^{d'}\frac{\partial\overline{u}_1'}{\partial x_3}\ \text{(SGS dissipation rate)}.$$

APPENDIX B

Numerical Treatment of the Single-Water-Column RANS Equation

The RANS equation governing the wind-driven flows studied here with modified KPP introduced in section 4 yield the following:

$$\nu\frac{du}{dz}+\nu_t'\frac{du}{dz}+\nu_t'\Gamma=u_{\tau w}^2, \tag{B1}$$

where z denotes the vertical extent of the water column ranging from $z=0$ at the bottom wall to $z=2\delta$ at the top surface. Recall that ν_t' is the depth-dependent (z dependent) modified KPP eddy viscosity, Γ is the countergradient flux accounting for nonlocal transport induced by full-depth LC (introduced in section 4c), and $u_{\tau w}$ is the friction velocity associated with the imposed wind stress at the top of the domain. For this configuration, in the mean, the bottom wall shear stress is equal to the wind stress. Solving Eq. (B1) for the mean downwind velocity gradient leads to an expression of the form

$$\frac{du}{dz}=f(z). \tag{B2}$$

Discretizing the z range $[0, 2\delta]$ into $N+1$ uniformly distributed grid points (and thus N grid cells of equal length Δz) and integrating Eq. (B2) over a grid cell extending from the point at $z=z_i$ to the point at $z=z_{i+1}$ leads to

$$u_{i+1}=u_i+\int_{z=z_i}^{z=z_{i+1}}f(z)\,dz. \tag{B3}$$

The bottom wall at $z=z_1=0$ is characterized by no-slip velocity; thus, $u_1=0$. Furthermore, the number of grid cells N is chosen such that the first grid point off the bottom wall ($z=z_2$) is located within the log layer. Evaluation of the integral in Eq. (B3) for the first grid cell adjacent to the wall (from $z=z_1$ to $z=z_2$) using the standard wall-function method (i.e., the wall model) described by Bredberg (2000) leads to direct specification of the velocity within the log layer, u_2, in accordance with the log law:

$$u_2=u_{\tau w}\left[\frac{1}{\kappa}\ln\left(\frac{u_{\tau w}z_2}{\nu}\right)+B\right]. \tag{B4}$$

Note that discussion on the importance of the B coefficient in Eq. (B4) when modeling flows with full-depth LC is given in section 5. The evaluation of the integral in Eq. (B3) for grid cells above the first cell can be performed numerically. For example, approximation of this integral with Simpson's rule leads to results nearly identical to the ANSYS Fluent model results presented in section 5.

REFERENCES

Akan, C., A. E. Tejada-Martínez, C. E. Grosch, and G. Martinat, 2013: Scalar transport in large-eddy simulation of Langmuir turbulence in shallowwater. *Cont. Shelf Res.*, **55**, 1–16, doi:10.1016/j.csr.2012.12.009.

Belcher, S. E., and Coauthors, 2012: A global perspective on Langmuir turbulence in the ocean surface boundary layer. *Geophys. Res. Lett.*, **39**, L18605, doi:10.1029/2012GL052932.

Bredberg, J., 2000: On the wall boundary condition for turbulence model. Internal Rep. 00/4, Dept. of Thermo and Fluid Dynamics, Chalmers University of Technology, Gothenburg, Sweden, 21 pp.

Craik, A. D. D., and S. Leibovich, 1976: A rational model for Langmuir circulations. *J. Fluid Mech.*, **73**, 401–426, doi:10.1017/S0022112076001420.

D'Alessio, S. J. D., K. Abdella, and N. A. McFarlane, 1998: A new second-order turbulence closure scheme for modeling the oceanic mixed layer. *J. Phys. Oceanogr.*, **28**, 1624–1641, doi:10.1175/1520-0485(1998)028<1624:ANSOTC>2.0.CO;2.

D'Asaro, E. A., 2014: Turbulence in the upper-ocean mixed layer. *Annu. Rev. Mar. Sci.*, **6**, 101–115, doi:10.1146/annurev-marine-010213-135138.

Frech, M., and L. Mahrt, 1995: A two-scale mixing formulation for the atmospheric boundary layer. *Bound.-Layer Meteor.*, **73**, 91–104, doi:10.1007/BF00708931.

Gargett, A. E., and J. R. Wells, 2007: Langmuir turbulence in shallow water. Part 1. Observations. *J. Fluid Mech.*, **576**, 27–61, doi:10.1017/S0022112006004575.

——, ——, A. E. Tejada-Martínez, and C. E. Grosch, 2004: Langmuir supercells: A mechanism for sediment resuspension and transport in shallow seas. *Science*, **306**, 1925–1928, doi:10.1126/science.1100849.

Harcourt, R. R., 2013: A second-moment closure model of Langmuir turbulence. *J. Phys. Oceanogr.*, **43**, 673–697, doi:10.1175/JPO-D-12-0105.1.

Holm, D., 1996: The ideal Craik-Leibovich equations. *Physica D*, **98**, 415–441, doi:10.1016/0167-2789(96)00105-4.

Kantha, L. H., and C. A. Clayson, 2004: On the effect of surface gravity waves on mixing in the oceanic mixed layer. *Ocean Modell.*, **6**, 101–124, doi:10.1016/S1463-5003(02)00062-8.

Kukulka, T., J. Plueddemann, J. H. Trowbridge, and P. P. Sullivan, 2011: The influence of crosswind tidal currents on Langmuir circulation in a shallow ocean. *J. Geophys. Res.*, **116**, C08005, doi:10.1029/2011JC006971.

——, ——, and P. P. Sullivan, 2012: Nonlocal transport due to Langmuir circulation in a coastal ocean. *J. Geophys. Res.*, **117**, C12007, doi:10.1029/2012JC008340.

Large, W. G., J. C. McWilliams, and S. C. Doney, 1994: Oceanic vertical mixing: A review and a model with a nonlocal boundary layer parameterization. *Rev. Geophys.*, **32**, 363–403, doi:10.1029/94RG01872.

Li, M., C. Garrett, and E. Skyllingstad, 2005: A regime diagram for classifying turbulent large eddies in the upper ocean. *Deep-Sea Res. I*, **52**, 259–278, doi:10.1016/j.dsr.2004.09.004.

Lilly, D. K., 1992: A proposed modification of the Germano subgrid-scale closure method. *Phys. Fluids*, **4A**, 633, doi:10.1063/1.858280.

McWilliams, J. C., and P. P. Sullivan, 2000: Vertical mixing by Langmuir circulations. *Spill Sci. Technol. Bull.*, **6**, 225–237, doi:10.1016/S1353-2561(01)00041-X.

——, ——, and C.-H. Moeng, 1997: Langmuir turbulence in the ocean. *J. Fluid Mech.*, **334**, 1–30, doi:10.1017/S0022112096004375.

——, E. Huckle, J. Liang, and P. Sullivan, 2012: The wavy Ekman layer: Langmuir circulations, breakers, and Reynolds stress. *J. Phys. Oceanogr.*, **42**, 1793–1816, doi:10.1175/JPO-D-12-07.1.

Papavassiliou, D. V. D. V., and T. J. T. J. Hanratty, 1997: Transport of a passive scalar in a turbulent channel flow. *Int. J. Heat Mass Transfer*, **40**, 1303–1311, doi:10.1016/S0017-9310(96)00202-5.

Phillips, O. M., 1967: *The Dynamics of the Upper Ocean*. 2nd ed. Cambridge University Press, 269 pp.

Pope, S. B., 2000: Turbulent Flows. 1st ed. Cambridge University Press, 802 pp.

Savidge, W., A. Gargett, R. Jahnke, J. Nelson, D. Savidge, R. T. Short, and G. Voulgaris, 2008: Forcing and dynamics of seafloor-water column exchange on a broad continental shelf. *Oceanography*, **21** (4), 179–184.

Skyllingstad, E. D., and D. W. Denbo, 1995: An ocean large-eddy simulation of Langmuir circulations and convection in the surface mixed layer. *J. Geophys. Res.*, **100**, 8501–8522, doi:10.1029/94JC03202.

Smyth, W. D., E. D. Skyllingstad, G. B. Crawford, and H. Wijesekera, 2002: Nonlocal fluxes and Stokes drift effects in the K-profile parameterization. *Ocean Dyn.*, **52**, 104–115, doi:10.1007/s10236-002-0012-9.

Teixeira, M. C., 2012: The influence of Langmuir turbulence on the scaling for the dissipation rate in the oceanic boundary layer. *J. Geophys. Res.*, **117**, C05015, doi:10.1029/2011JC007235.

Tejada-Martínez, A. E., and C. E. Grosch, 2007: Langmuir turbulence in shallow water. Part 2. Large-eddy simulation. *J. Fluid Mech.*, **576**, 63–108, doi:10.1017/S0022112006004587.

——, ——, A. E. Gargett, J. A. Polton, J. A. Smith, and J. A. MacKinnon, 2009: A hybrid spectral/finite-difference large-eddy simulator of turbulent processes in the upper ocean. *Ocean Modell.*, **30**, 115–142, doi:10.1016/j.ocemod.2009.06.008.

——, ——, N. Sinha, C. Akan, and G. Martinat, 2012: Disruption of bottom log-layer in LES of full-depth Langmuir circulation. *J. Fluid Mech.*, **699**, 79–93, doi:10.1017/jfm.2012.84.

——, C. Akan, N. Sinha, C. E. Grosch, and G. Martinat, 2013: Surface dynamics in LES of full-depth Langmuir circulation in shallow water. *Phys. Scr.*, **T155**, 014008, doi:10.1088/0031-8949/2013/T155/014008.